

Dynamic-frequency technique for speeding up bubble growth

Shengcai Li*

School of Engineering, Warwick University,
Coventry, UK CV4 7AL

Yuning Zhang

School of Engineering, Warwick University,
Coventry, UK CV4 7AL

*S.Li@warwick.ac.uk

ABSTRACT

A dynamic-frequency approach, for which driving frequency follows resonant frequency of bubbles, is offered in present paper for achieving quickest bubble growth in acoustic field. Its advantages are demonstrated by comparing with the constant-frequency technique based on their rectified diffusion.

1. INTRODUCTION

Rectified diffusion is a process of bubble dissolution or growth in acoustic fields. This process involves in many medical and bioengineering applications where bubbles are generated in sound field and their growth rate is a primary concern. For such applications, a technique that generates a sound field with its frequency following the decreasing value of the resonant frequency of the growing bubbles (i.e. dynamic-frequency technique) has been proposed by Li in 2008 [1]. In order to demonstrate the advantage of this technique, examples will be given for growing gas bubbles near resonance.

For detail information of rectified diffusion, readers are referred to Crum [2]. As far as analytic work on the subject, Crum and Hansen [3] derived the first generalized equations by introducing the polytropic exponent and all three damping terms (i.e. viscous, thermal and acoustic dampings) which were obtained earlier by Devin [4] and Eller [5]. Near resonance, thermal damping is a dominant damping mechanism for gas bubble oscillating in liquids. For thermal effects, formulas in Devin [4] can be reduced based on the framework of Prosperetti [6] as demonstrated by Crum [7]. Recently, Prosperetti's framework [6] has been applied to higher frequency range that used in medical and bioengineering applications [8].

The growth of bubble will attain the maximum rate at/near resonant frequency. The approach in Crum and Hansen [3] has been used for the demonstrations presented in this paper with Eqs. (14)-(17) in Prosperetti [6] for calculations of thermal effects. The predicted bubble growth rate by the dynamic-frequency technique is compared with that by the constant-frequency technique for some typical cases, showing its superiority over the constant-frequency technique.

2. RESULTS AND DISCUSSIONS

In this section, demonstrating examples are shown for air bubbles in water with details given in Appendix. For the dynamic-frequency technique, the driving frequency (ω) follows the variation of resonant frequency (ω_r) of the growing bubbles to achieve the fastest growth rate at the status of resonance while the driving frequency (ω) for the constant-frequency technique is equal to resonant frequency (ω_r) of the initial bubble. Here, the resonance frequency is defined as the maximum responding magnitude of oscillating gas bubbles for given amplitude of sound field [9]. For many biomedical applications, bubbles are in the range of 1-10 μm , which are chosen for the following demonstrating examples. Fig.1 compares the instant equilibrium bubble radius and its bubble growth rate for the dynamic-frequency and the constant-frequency techniques respectively. The initial equilibrium bubble radius (R_0) is 2 μm , corresponding to a resonant frequency $\omega_r = 1.04 \times 10^7 \text{ sec}^{-1}$ [9]. For the constant-frequency approach, the bubble stops growing soon after the resonant frequency (ω_r) of bubbles deviating from the driving frequency (ω). Whereas, for the dynamic-frequency approach, the bubble grows much quicker since the driving frequency (ω) always follows the reducing resonant frequency (ω_r) of bubbles.

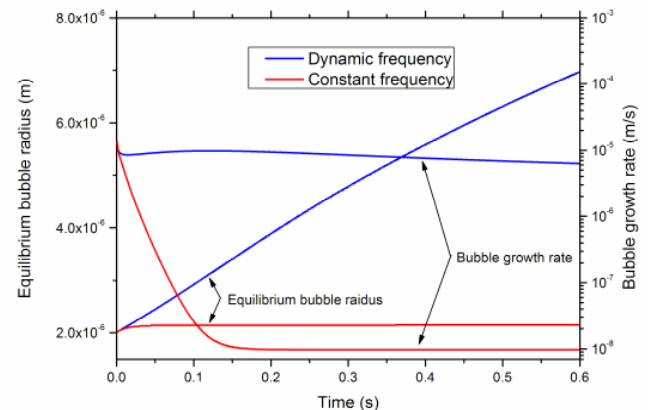


Fig.1 Comparison of equilibrium bubble radius and bubble growth rate predicted by the dynamic-frequency and the constant-frequency techniques. The initial R_0 is 2 μm , corresponding to a resonant frequency $\omega_r = 1.04 \times 10^7 \text{ sec}^{-1}$. For

the constant-frequency technique, its driving frequency is set as ω_r .

For practical applications, the driving frequency (ω) may vary in steps. Fig.2 shows the effect of step-change in the driving frequency. Even finite steps of frequency change ($i=2$ or 5, here i is the total number of frequencies used in the dynamic-frequency approach) will accelerate bubble growth considerably.

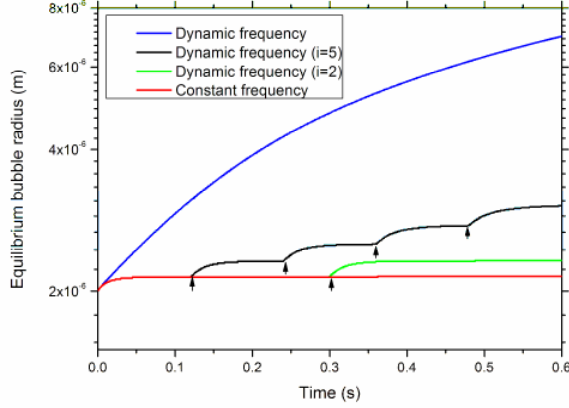


Fig.2 Comparison of the dynamic-frequency (in step change) with the constant-frequency technique. Arrows indicate the instance of the step change in frequency.

Table 1 shows the comparisons of the final equilibrium bubble radius for a short duration of 60 ms. Three cases of initial bubble radii ($R_0=2, 5$ and $10 \mu\text{m}$) are tested, representing some typical sizes of bubbles in biomedical applications. Dynamic frequency approach is more effective for small bubbles (e.g. $R_0=2$ and $5 \mu\text{m}$) but less effective for large bubbles (e.g. $R_0=10 \mu\text{m}$). Whereas for longer duration, say 6s, for the large bubble ($R_0=10 \mu\text{m}$) the acceleration effect will manifest itself eventually, giving a final equilibrium bubble radius of $27.6 \mu\text{m}$ against $12.9 \mu\text{m}$ (referring to Table 2).

Table 1. Comparisons of the final equilibrium bubble radius with time duration of 60 ms.

Method	$R_0=2 \mu\text{m}$	$R_0=5 \mu\text{m}$	$R_0=10 \mu\text{m}$
Constant frequency	2.14 μm	5.46 μm	10.5 μm
Dynamic frequency	2.54 μm	5.70 μm	10.5 μm
Dynamic frequency ($i=2$)	2.26 μm	5.58 μm	10.5 μm

Table 2. Comparisons of the final equilibrium bubble radius with time duration of 6 s.

Method	$R_0=2 \mu\text{m}$	$R_0=5 \mu\text{m}$	$R_0=10 \mu\text{m}$
Constant frequency	2.15 μm	5.96 μm	12.9 μm
Dynamic frequency	24.2 μm	25.3 μm	27.6 μm
Dynamic frequency ($i=2$)	2.32 μm	7.18 μm	15.3 μm

The dynamic-frequency technique has great potential for accelerating bubble growth in many applications. However, a novel device capable of generating a variable driving frequency is essential for the implementation of this approach.

3. CONCLUSIONS

A dynamic-frequency technique proposed in 2008 has been briefly described together with demonstrating examples for the growth of acoustic bubbles. The driving frequency follows the instant value of the resonant frequency of the growing bubbles such that the quickest growth rate can be achieved. To implement this technique, a novel device for generating sound field with variable frequency is to be developed.

ACKNOWLEDGEMENT

This work has been supported by UK EPSRC WIMRC grant (RESCM 9219) and EPSRC WIMRC PhD studentship (RESCM 9217).

REFERENCES

- [1] Li, S. C. (2008). Minutes of WIMRC cavitation project (Phase II, Major 48), Group meeting, 24 March 2008, Warwick University,
- [2] Crum, L. A. (1984). "Acoustic cavitation series: part five rectified diffusion," *Ultrasonics*, **22**, 215-223.
- [3] Crum, L. A. and Hansen, G. M. (1982). "Generalized equations for rectified diffusion," *J. Acoust. Soc. Am.* **72**, 1586-1592.
- [4] Devin, C. (1959). "Survey of thermal, radiation, and viscous damping of pulsating air bubbles in water," *J. Acoust. Soc. Am.* **31**, 1654-1667.
- [5] Eller, A. I. (1970). "Damping constants of pulsating bubbles," *J. Acoust. Soc. Am.* **47**, 1469-1470.
- [6] Prosperetti, A. (1977). "Thermal effects and damping mechanisms in the forced radial oscillations of gas bubbles in liquids," *J. Acoust. Soc. Am.* **61**, 17-27.
- [7] Crum, L. A. (1983). "The polytropic exponent of gas contained within air bubbles pulsating in a liquid," *J. Acoust. Soc. Am.* **73**, 116-120.
- [8] Zhang, Y. and Li, S. C. (2010). "Notes on radial oscillations of gas bubbles in liquids: Thermal effects," *J. Acoust. Soc. Am.*, **128**, EL306-309.
- [9] Brennen, C. E. (1995). *Cavitation and bubble dynamics* (Oxford University Press, New York), Chapter 4.2, pp.115.
- [10] Crum, L. A. (1980). "Measurements of the growth of air bubbles by rectified diffusion," *J. Acoust. Soc. Am.* **68**, 203-211.

APPENDIX

The following values are used for calculating the examples with most notations used in Prosperetti [6] and Crum and Hansen [3]: ambient pressure $P_\infty = 1.01 \times 10^5 \text{ Pa}$; surface tension $\sigma = 68 \text{ dyn/m}^1$; liquid density $\rho_l = 1000 \text{ kg/m}^3$; sound speed in liquids $c_l = 1486 \text{ m/s}$; liquid viscosity $\mu_l = 0.001 \text{ Pa}\cdot\text{s}$; diffusion constant $D = 2.4 \times 10^{-9} \text{ m}^2/\text{s}$; thermal diffusivity of the gas at constant pressure $D_{g,p} = 2.08 \times 10^{-5} \text{ m}^2/\text{s}$; thermal diffusivity of the gas at constant volume $D_{g,v} = 2.90 \times 10^{-5} \text{ m}^2/\text{s}$; thermal diffusivity of the liquids $D_l = 1.42 \times 10^{-7} \text{ m}^2/\text{s}$; gas thermal

¹ This value was measured by Crum [10] and used in [3, 10].

conductivity $k_g = 2.54 \times 10^3$ erg/cm/sec/K; liquid thermal conductivity $k_l = 5.9 \times 10^4$ erg/cm/sec/K; specific heat ratio $\gamma = 1.40$; universal gas constant $R_g = 8.314$ J/mol/K; molecular weight of the gas in bubble $M_g = 28.88$ g; absolute temperature $T = 293$ K; coefficient $d = R_g T C_0 / P_\infty = 0.02$ (C_0 is saturation concentration of gas in liquid in moles/unit volume); amplitude of acoustic pressure $P_A = 3.3 \times 10^4$ Pa; ratio between gas concentration and saturation concentration in liquid $C_i / C_0 = 1$.

Characterization of the jet in collapsing bubble induced pumping in viscous fluids

Badarinath Karri*

NUS Graduate School for Integrative Sciences
and Engineering, Center for Life Sciences, #05-
01, 28 Medical Drive, Singapore 117456

Evert Klaseboer

Institute of High Performance Computing (IHPC),
1 Fusionopolis Way, #16-16 Connexis, Singapore
138632

Boo Cheong Khoo

Department of Mechanical Engineering, National
University of Singapore, Kent Ridge Singapore
119260

Ong Zhao Lin

Department of Mechanical Engineering, National
University of Singapore, Kent Ridge Singapore
119260

Siew-Wan Ohl

Institute of High Performance Computing (IHPC),
1 Fusionopolis Way, #16-16 Connexis, Singapore
138632

*badarinath@nus.edu.sg

ABSTRACT

The collapsing bubble induced pump makes use of the jet formed in a non-equilibrium bubble oscillating near a perforated wall to pump fluid from one side of the wall to another through the hole. The pump has no moving parts which makes it advantageous for use at the microscale such as in lab-on-a-chip or microfluidic devices because of the fragility and difficulties of fabricating parts such as valves at that scale. In the present work, the characteristics of the high speed jet for such a pump are studied especially when viscosity becomes important. Solutions of different viscosity are obtained by varying the concentration of glycerine in water by volume. A bubble is created in the fluid using a low-voltage electrical spark, close to a fixed perforated plate and the dynamics of the bubble and subsequent pumping are recorded using a high-speed camera. To characterize the jet, firstly the non-dimensional groups governing the pumping are identified via dimensional analysis. The experimental data from the high-speed video images are used to obtain the position of the jet tip as it varies with time and the jet velocity at the entrance to the hole is calculated. The non-dimensional bubble-centre to plate distance at which the jet fails to form is compared with the non-dimensional distance at which the pumping fails. Results show the jet characteristics to be dependent on two key parameters, the non-dimensional bubble centre to plate distance and the Reynolds number for a given holed plate.

NOMENCLATURE

R_m	Maximum radius of the bubble
L	Thickness of the plate used
H	Dimensional distance from the top of the plate to the center of the bubble
R_h	Radius of the hole in the plate
H'	Non-dimensionalized H given by $H' = H/R_m$

H'_{lim}	Minimum H' at which the jet fails to reach the plate
H'_{crit}	Minimum H' at which the jet fails to form
μ	Dynamic viscosity of the fluid given in mPas
ρ	Density of fluid used in kg/m^3
p_0	Pressure in the surrounding fluid near a bubble
Re	Reynolds number
E	Efficacy of pumping

1. INTRODUCTION

An oscillating bubble in a non-uniform flow field forms a high-speed jet upon collapse. Such jets are observed in bubbles subject to an impinging shock-wave or a bubble near a free surface or a rigid boundary. Bubbles near a rigid boundary collapse with a jet towards the boundary and have been studied both experimentally [1-3] and numerically [4-7] due to their importance in studying cavitation damage. In recent years, the bubble induced jets have been used for more constructive applications such as studying poration into cells [8-9], jet induced pumping [10-13], and bubbles near biomaterials [14], to name a few.

One such application of the bubble induced jet is in a collapsing bubble induced pump. A bubble is created near a rigid wall with a hole and collapses with a jet towards the boundary. Consequently, fluid is pumped from one side of the wall to another through the hole. The pump thus obtained has the advantage of having no moving parts. The principle behind this collapsing bubble induced pump was first shown numerically by Khoo et al. [10], and has subsequently been demonstrated experimentally for water by Lew et al. [11], at the micro-scale by Dijkink and Ohl [12] and recently in the pumping of viscous fluids by Karri et al. [13].

The high-speed jet formed during bubble collapse plays a key role in the pumping effect. As such, the formation of the high-speed jet and its characteristics such as its impact velocity

on the boundary are dependent on the non-dimensional distance between the bubble center and the rigid plate, H' . In previous studies on jet characteristics, Philipp and Lauterborn [2] have experimentally shown a wide variety of jets in terms of jet shape and size with change in H' . Pearson et al. [6] have calculated numerical quantities associated with the jet such as the jet Kelvin impulse and kinetic energy. The studies [2,6] however used water as the fluid medium and a bubble located near a rigid boundary without a hole. For viscous fluids, Popinet and Zaleski [15] have numerically studied the parameters influencing jet formation in a bubble near a wall. The effect of viscosity on the jet velocity has also been numerically studied for fluids of two different viscosities by Minsier et al. [16]. Experimental studies in viscous fluids have however been limited to spherical bubbles [17-19] and the characteristics of a jetting bubble in viscous fluids has not been studied. This provides the motivation for the present study.

2. EXPERIMENTAL SET-UP

The experimental set-up used in this study is shown in Figure 1. It consists of a glass tank to hold the liquid, an electrical circuit to create the bubble using a low-voltage spark, a plate with a hole and a high-speed camera and illumination system to record the bubble dynamics.

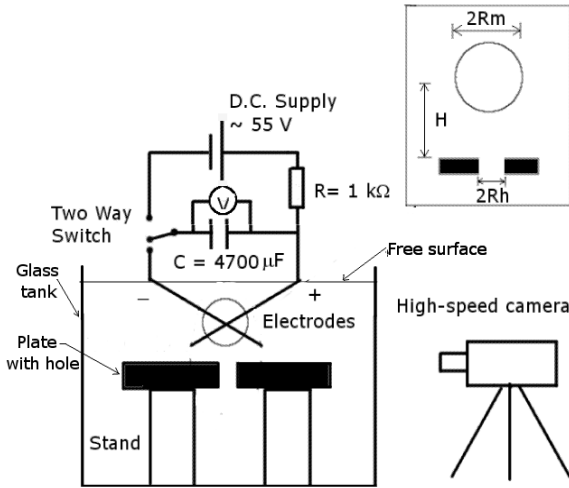


Figure 1. The experimental set-up used in the present study. The bubble related dimensions are shown in the rectangular box on the top right.

The glass tank is of size 180 mm x 190 mm x 200 mm and is filled with the fluid up to a height of 170 mm. The electrical circuit comprises of a capacitor of 4700 μ F in series with a resistor of 1 k Ω and connected to a DC power supply. The capacitor is charged to a voltage of \sim 55 V measured using a voltmeter and then discharged through two crossed electrodes, made of thin copper wires \sim 0.1 mm in diameter. The discharge of the capacitor through the electrodes creates a spark which leads to an expanding bubble. A plate of size 80 mm x 70 mm with a thickness $L = 5$ mm and a hole of radius $R_h = 2.5$ mm at its center is placed in the liquid below the crossed electrodes.

The plate is held in place using a custom-built stand comprising four aluminum cylinders to which the plate is screwed.

Fluids of different viscosity were obtained by varying the concentration of glycerin in water. The viscosity of the solution was measured before and after the experiments for each fluid using a rotating cylinder viscometer (RION Viscotester VT-03F/04F) and the variation was found to be minimal [5-10%]. Three different solutions of viscosities $\mu = 45$ mPas, 75 mPas, and 900 mPas were used in the present study. Experiments were also conducted in water ($\mu = 1$ mPas) for comparison. A high-speed camera (Photron FASTCAM APS-RX / SA 1.1) was used for recording the bubble dynamics with frame rates up to 225000 frames per second. The calibration of the images was done using a ruler imaged at the focus of the camera.

3. STUDY OF JET CHARACTERISTICS

In this section, a dimensional analysis is first presented which identifies Reynolds number Re and the non-dimensional distance H' as the key parameters that influence the pumping. Subsequently, the experimental results on the high speed jet are presented in two parts. First, high-speed images of two examples of bubbles in water and another viscous fluid are presented. The examples illustrate some characteristics of the jet as viscosity changes. The variation of the jet characteristics in terms of its formation and pumping failure is then quantified in terms of H' and Reynolds number Re . This is followed by results showing the variation of the jet velocity at the entrance to the hole for different viscous fluids.

3.1 DIMENSIONAL ANALYSIS

The pumping due to the collapsing bubble is affected by parameters such as the distance of the bubble-center from the plate H , the maximum radius of the bubble R_m , the radius of the hole in the plate R_h , the plate thickness L , and the inherent fluid properties, such as surrounding reference pressure p_0 , density ρ and dynamic viscosity μ . This can be expressed in mathematical terms as

$$E = f(p_0, \rho, \mu, R_m, R_h, H, L) \quad (1)$$

where E is the efficacy of pumping. A dimensional analysis to obtain the dimensionless groups is carried out using p_0 , ρ and R_m as the repeating terms. This gives the pumping efficacy as

$$E = f(Re, H', L', R_h/R_m) \quad (2)$$

Here Re is the Reynolds number defined as

$$Re = \sqrt{\frac{p_0}{\rho}} \frac{\rho R_m}{\mu} \quad (3)$$

and L' is given by

$$L' = \frac{L}{R_m} \quad (4)$$

The characteristic velocity of the system appears as

$$v_{bub} = \sqrt{\frac{p_0}{\rho}} \quad (5)$$

as used in the Reynolds number definition in Equation 3.

For a given plate of fixed hole radius R_h and thickness L , the dimensionless terms R_h/R_m and L' are constants if the bubble size R_m is kept unchanged. In such a case, the efficacy E defined in Equation 2 is a function varying only with Re and H' . In a similar way, other dimensionless flow parameters are deemed likely to be dependent on Re and H' . In the experiments presented here, the variation of the bubble radius R_m was within the limited range of 4 mm to 5.5 mm irrespective of the viscosity of the fluid used. For simplicity of analysis, the R_m is therefore taken to be a constant.

It should be noted that the effect of the heat and mass transfer from the bubble to the surrounding fluid and the effect of surface tension on the bubble surface upon the efficacy of pumping has been neglected in the above analysis. This is justified as follows.

If we consider the time-scales of the bubble oscillation and collapse and its lifetime, the typical time scale t_{bub} is of the order of a few milliseconds for the bubbles used in our study. For heat transfer to the surrounding fluid, a typical value of the thermal penetration depth over which heat transfer takes place in time t_{bub} is given by $L_{th} \sim \sqrt{D_t t_{bub}}$ in water, where $D_t = 1.6 \times 10^{-7} \text{ m}^2/\text{s}$ is the coefficient of thermal diffusivity of water at a temperature of 300 K. Substituting a value of $t_{bub} = 1 \text{ ms}$, this gives $L_{th} \sim 12 \text{ } \mu\text{m}$ which is 100 times smaller than the bubble radius of the order of 1 mm in our experiments. As such, heat transfer effect is not likely to be important. A similar analysis can be carried out for the typical length scale L_m for mass transfer by diffusion in water and given as $L_m \sim \sqrt{D_m t_{bub}}$. Here D_m is the mass diffusivity coefficient of water and with a typical value of $D_m = 10^{-9} \text{ m}^2/\text{s}$, this gives rise to $L_m \sim 1 \text{ } \mu\text{m}$ which is 1000 times smaller than the bubble radius of the order of 1 mm. Hence mass transfer is also neglected.

For the surface tension, its effect in terms of pressure is given by $p_s = 2\sigma/R$, where σ is the coefficient of surface tension and R is the bubble radius. A comparison between the pressure caused by the oscillating bubble which is typically given as $p_{bub} = 1/2 \rho v^2$ and the surface tension term p_s is presented next.

Consider the characteristic velocity $v_{bub} = 10 \text{ m/s}$ with p_0 at 10^5 N/m^2 and density $\rho = 1000 \text{ kg/m}^3$, using which we get the bubble pressure term as $p_{bub} = 5 \times 10^4 \text{ Pa}$. For a surface tension coefficient of $\sigma = 73 \times 10^{-3} \text{ N/m}$ (applicable for water-air interface), and a bubble radius R of the order of 1 mm, the surface tension term $p_s = 146 \text{ Pa}$, which is two orders of magnitude lower compared to p_{bub} . Hence surface tension has been neglected. For a micron sized bubble, the surface tension pressure term p_s would be of the same order of magnitude as p_{bub} . Therefore the effect of surface tension would become more important for micron sized bubbles and can be neglected for millimeter sized bubbles as employed in the present experiments.

The effect of the surface tension for such similar sized non-equilibrium bubbles in millimeter has also been shown to be negligible in an earlier study by Fong et al. [20].

3.2 QUALITATIVE DIFFERENCES IN JET CHARACTERISTICS DUE TO VISCOSITY

In order to characterize the jet, first the changes in the jet due to change in viscosity as observed from the high-speed video images is presented. Karri et al [13] in a recent paper have described in detail the variation of the collapsing bubble induced pumping through a holed plate as the viscosity is varied. Specifically, it was observed that an increase in viscosity leads to a bubble which simultaneously oscillates and translates towards the hole and doesn't break up into smaller bubbles unlike the case in water. At higher viscosities, jet formation was also suppressed.

One specific characteristics of the jet as the viscosity increases is shown through a comparison between Figures 2 and 3. Figure 2 shows an example of a bubble in water ($\mu = 1 \text{ mPas}$) while Figure 3 shows a bubble in a solution of $\mu = 900 \text{ mPas}$ at a similar H' as that in Figure 2.

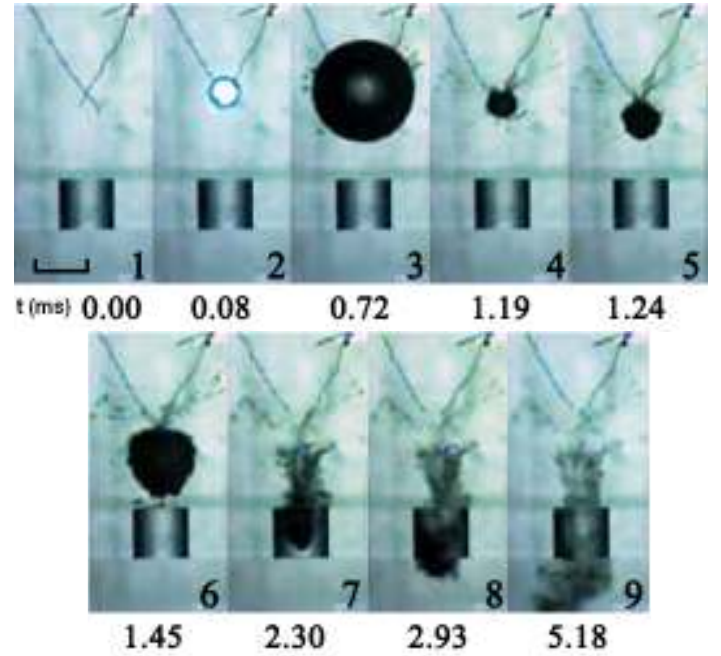


Figure 2. A collapsing bubble in water with $H' = 1.64$ and a maximum radius $R_m = 5 \text{ mm}$ (Frame 3). The bubble collapses and enters the hole in Frame 6. By Frame 9, the bubble has completely disintegrated leaving a number of small bubbles in its wake. Note that only 2 oscillations of the bubble are observed. The scale bar in Frame 1 shows a length of 5 mm. The times corresponding to each frame are indicated below the frame.

For water (Fig. 2), the bubble collapses and fully enters into the hole pumping fluid and by the end of pumping, the bubble completely disintegrates. However for the fluid of viscosity $\mu = 900 \text{ mPas}$ (Fig. 3), the jet that forms in the bubble (Frame 6), breaks away from the bubble into a thin jet (Frames 7 to 9) when the main bubble starts shrinking in its oscillation cycle. This break-up of a thin jet has been observed for all the three viscous fluids studied ($\mu = 45 \text{ mPas}$, 75 mPas and 900 mPas) when the H' is greater than 1.5.

For all the viscous fluids used the jet that breaks away moves into the hole first as a thin jet. Subsequently, the main bubble moves into the hole at a later time while oscillating and translating towards the hole (as shown in Fig. 3, Frames 10-12). It appears that the presence of the hole plays an important role in the jet break-up. The bubble elongates towards the hole during its second or third expansion cycle and in the ensuing collapse cycle, the jet breaks away while the bubble shrinks. A possible reason for the occurrence of this jet-break up at $H' > 1.5$ is that in such cases, the bubble remains outside the hole as it oscillates. For $H' < 1.5$, the main bubble itself enters the hole along with the jet and the jet doesn't break away as the bubble now oscillates within the hole.



Figure 3. A collapsing bubble in a fluid of viscosity $\mu = 900$ mPas at a non-dimensional distance $H' = 1.5$. The maximum radius of the bubble is $R_m = 4.9$ mm (Frame 3). The jet from the bubble enters the hole in Frame 5. Note the break-up of the jet from the main bubble in Frame 7 as the main bubble shrinks in its oscillation cycle. The scale bar shown in Frame 1 corresponds to 5 mm.

3.3 VARIATION OF JETTING WITH H' AND Re

In order to characterize the pumping and jet characteristics in terms of the key non-dimensional parameters identified in Section 3.1, we define two specific non-dimensional bubble center to plate distances H' , namely H'_{lim} and H'_{crit} as follows. H'_{lim} is defined as the non-dimensional distance at which the pumping fails. The failure can occur because the jet doesn't translate enough to reach the plate or in cases when the jet is suppressed, the bubble doesn't translate enough to reach the plate and pump fluid [13]. H'_{crit} refers to the minimum non-dimensional distance at which the bubble fails to form a jet. As the non-dimensional distance H' increases, the bubble begins to oscillate spherically like a free-field bubble as it no longer feels the presence of the plate. The distance H' when the bubble first starts oscillating spherically is defined as H'_{crit} and it depends on the viscosity of the fluid used.

In Figure 4, H'_{crit} and H'_{lim} for different experimental runs are plotted with respect to the Reynolds number Re for the corresponding experimental run. The Reynolds number Re is calculated using Equation 3 where p_0 is the surrounding pressure taken as 10^5 Pa and $\rho = 1000$ kg/m³.

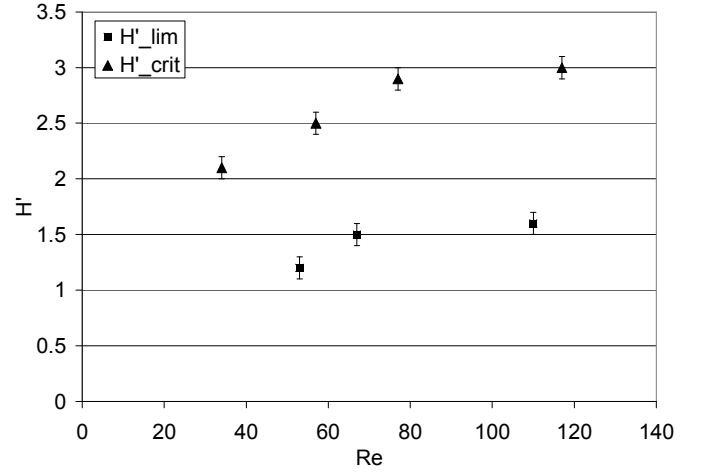


Figure 4. Plot of the H'_{crit} and H'_{lim} with the Reynolds number Re obtained from Equation 3 for different experimental runs. The H'_{crit} values are higher than the H'_{lim} values as is to be expected. There seems to be a difference in the variation of H'_{lim} and H'_{crit} , for $Re < 80$ and $Re > 80$.

From Figure 4, both H'_{lim} and H'_{crit} show a similar variation with Reynolds number. There is a greater increase in H' (limiting or critical) with increase in Re for $Re < 80$ while for $Re > 80$, the increase is gradual. It is noted that a decrease in Re can happen due to a decrease in the bubble size (R_m) or an increase in the viscosity μ . For a bubble of $R_m = 5.0$ mm, the value of $Re = 80$ corresponds to a viscosity of $\mu = 625$ mPas. Thus at viscosities higher than this value, the effect of viscosity on pumping (given by H'_{lim}) and jet formation (given by H'_{crit}) is expected to be significant. As such, H'_{crit} is expected to be higher than H'_{lim} . This is because in evaluating H'_{lim} , the jet forms but fails to reach the plate while for H'_{crit} the jet no longer forms.

A second characteristic of the jet is the velocity of the jet at the entrance to the hole. Figure 5 shows the variation of this entry velocity of the jet with variation in H' for fluids of viscosities $\mu = 1$ mPas, 45 mPas, 75 mPas and 900 mPas. The values of $H' > 1$ are considered here because for $H' < 1$, the jet is already within the hole when the bubble collapses. From Figure 5, it is noted that as the H' increases, the velocity of the jet at the hole decreases. This is because at a higher H' , the distance that the jet has to travel to reach the hole increases and correspondingly it gets decelerated by the resistance offered by the fluid. Figure 5 also indicates that the velocity of the jet and its variation is similar for all the fluids used.

4. CONCLUSIONS

The high speed jet formed in a collapsing bubble near a holed plate plays an important role in bubble induced pumping and the characteristics of this high speed jet have been studied. A dimensional analysis to evaluate the non-dimensional

parameters that affect the collapsing bubble induced pumping shows that for a given plate, the Reynolds number Re and the

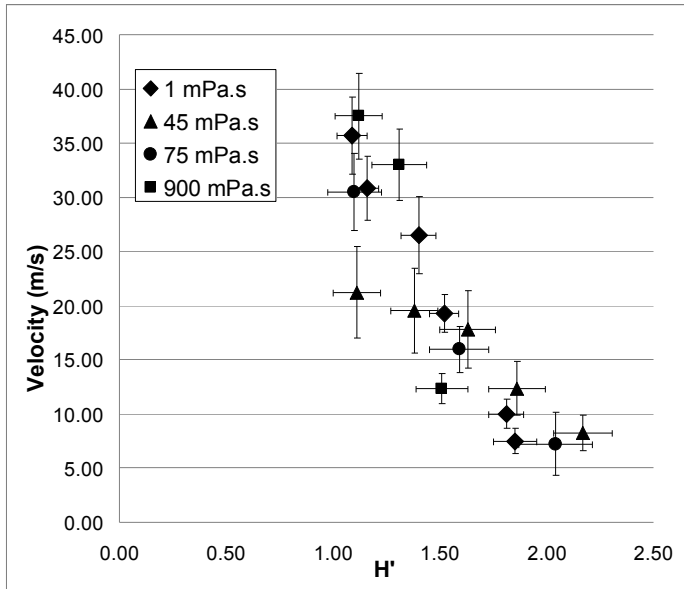


Figure 5. Plot of the variation of the jet velocity at the entrance of the hole with respect to H' for fluids of different viscosities.

non-dimensional distance of the bubble center from the plate H' are the key parameters affecting pumping. The jet characteristics are studied both qualitatively and in terms of the variation of the H'_{lim} (pumping) and H'_{crit} (jet formation) with the Reynolds number Re . The variation of the jet velocity at the entrance to the hole with viscosity and H' is also presented.

REFERENCES

[1] Y. Tomita and A. Shima, "Mechanisms of impulsive pressure generation and damage pit formation by bubble collapse," *Journal of Fluid Mechanics*, vol. 169, pp. 535-564, 1986.

[2] A. Philipp and W. Lauterborn, "Cavitation erosion by single laser-produced bubbles," *Journal of Fluid Mechanics*, vol. 361, pp. 75-116, 1998.

[3] N. D. Shutler and R. B. Mesler, "A photographic study of the dynamics and damage capabilities of bubbles collapsing near solid boundaries," *Transactions of ASME Series D, Journal of Basic Engineering*, vol. 87, pp. 511-517, 1965.

[4] M. S. Plesset and R. B. Chapman, "Collapse of an initially spherical vapor cavity in the neighborhood of a solid boundary," *Journal of Fluid Mechanics*, vol. 47, pp. 283-290, 1971.

[5] J. R. Blake, B. B. Taib, and G. Doherty, "Transient cavities near boundaries. Part 1. Rigid boundary," *Journal of Fluid Mechanics*, vol. 170, pp. 479-497, 1986.

[6] A. Pearson, J. R. Blake, and S. R. Otto, "Jets in bubbles," *Journal of Engineering Mathematics*, vol. 48, pp. 391-412, 2004.

[7] J. P. Best and A. Kucera, "A numerical investigation of non-spherical rebounding bubbles," *Journal of Fluid Mechanics*, vol. 245, pp. 137-154, 1992.

[8] C.-D. Ohl, M. Arora, R. Ikink, N. de Jong, M. Versluis, M. Delius, and D. Lohse, "Sonoporation from jetting cavitation bubbles," *Biophysical Journal*, vol. 91, pp. 4285-4295, 2006.

[9] G. Sankin, F. Yuan, and P. Zhong, "Pulsating tandem microbubble for localized and directional single-cell membrane poration," *Physical Review Letters* 105, 078101 (2010).

[10] B. C. Khoo, E. Klaseboer, and K. C. Hung, "A collapsing bubble-induced micro-pump using the jetting effect," *Sensors and Actuators A*, vol. 118, pp. 152-161, 2005.

[11] K. S. F. Lew, E. Klaseboer, and B. C. Khoo, "A collapsing bubble-induced micropump: An experimental study," *Sensors and Actuators A*, vol. 133, pp. 161-172, 2007.

[12] R. Dijkink and C.-D. Ohl, "Laser-induced cavitation based micropump," *Lab on a Chip*, vol. 8, pp. 1676-1681, 2008.

[13] B. Karri, K. S. Pillai, E. Klaseboer, S.-W. Ohl, and B. C. Khoo, "Collapsing bubble induced pumping in a viscous fluid," *Sensors and Actuators A*, 2011 doi:10.1016/j.sna.2011.04.015 (In Press)

[14] S. W. Fong, E. Klaseboer, C. K. Turangan, B. C. Khoo, and K. C. Hung, "Numerical analysis of a gas bubble near bio-materials in an ultrasound field," *Ultrasound in Medicine and Biology*, vol. 32, no. 6, pp. 925-942, 2006.

[15] S. Popinet and S. Zaleski, "Bubble collapse near a solid boundary: a numerical study of the influence of viscosity," *Journal of Fluid Mechanics*, vol. 464, pp. 137-163, 2002.

[16] V. Minsier, J. de Wilde, and J. Proost, "Simulation of the effect of viscosity on jet penetration into a single cavitating bubble," *Journal of Applied Physics*, vol. 106, no. 084906, 2009.

[17] F. Jomni and A. Dénat, "Viscosity effect on the dynamics of small bubbles generated by electrical current pulse in viscous insulating liquids," *Conference on Electrical Insulation and Dielectric Phenomena, IEEE 1997 Annual Report*, vol. 2, pp. 652-655, Oct 1997.

[18] A. R. McCarn, E. M. Englert, and G. A. Williams, "Laser induced bubbles in glycerol-water mixtures," *American Physical Society (APS) March Meeting*, 2008.

[19] G. A. Williams, "Physics and chemistry of luminescence from laser-induced bubbles in liquids," *Conference on Cavitation: Turbomachinery and Medical Applications, WIMRC Forum*, 2008.

[20] S. W. Fong, E. Klaseboer, and B. C. Khoo, "Interaction of microbubbles with high intensity pulsed ultrasound," *Journal of Acoustical Society of America*, vol. 123, pp. 1784-1793, 2008.

A novel dual-sensor approach for the determination of cavitation in-vitro

Ian Butterworth, Mark Hodnett and Christian Baker
National Physical Laboratory, Teddington, UK

Background

With both the positive and detrimental effects of cavitation attracting increasing interest for biomedical applications, it is crucial that the dynamics of cavitation within tissue are characterised to optimise, and minimise the uncertainty in, cavitation critical processes. During high intensity focussed ultrasound (HIFU) treatments, cavitation is becoming an increasingly significant factor; for example, under conditions where the ultrasonic thermal dose conditions required for tissue necrosis exceeds the rarefactional (peak-negative) acoustic pressure threshold for cavitation. This cavitation can cause additional mechanical damage to the tissue, whilst also acting as strong acoustic reflectors for the incoming HIFU field, resulting in significant perturbation of the field. Early detection of cavitation, or prediction, is therefore of clear clinical benefit.

Outline

This work investigated the *in-vitro* application of a novel cylindrically focused broadband cavitation detector, in conjunction with a miniature fibre-optic hydrophone, to locally detect the HIFU field and simultaneously monitor generated cavitation emissions, thereby enabling the correlation of the two detector responses.

Material & Methods

Studies were made using a tone burst 1.1 MHz HIFU field, as a function of acoustic pressure at the focus. The cylindrical cavitation sensor was filled with a tissue-like medium, with the HIFU beam focus aligned to its acoustic centre. The fibre-optic hydrophone was placed close to the focus of the acoustic field, to provide a measure of the local acoustic pressures. Characterisation of the cavitation activity was provided through three indicators, based on multiband integration of the outputs from the two sensors. These quantified three distinct cavitation characteristics, while rejecting non-linear harmonics of the HIFU field, providing levels of *sub-harmonic*, *fractional* and *broadband* acoustic cavitation emissions.

Results

Levels of cavitation emissions were compared to the acoustic pressure at the focus, through the successful adoption of this dual-sensor approach.

The tissue mimics were exposed to acoustic fields whose modulus of the peak-rarefactional acoustic pressure was greater than 5 MPa, conditions where high levels of cavitation were observed, and distinct thresholds of cavitation identified through the developed indicators. The cylindrical sensor output signal was seen to be very sensitive to both the inertial cavitation emissions and the resulting reflections of the HIFU field, providing a clear indication of the onset of cavitation.

Overall, the dual-sensor approach has provided a clear indication of cavitation threshold for *in-vitro* characterisation of tissue mimics, and therefore lends itself well to aiding the prediction of biomedical cavitation activity.

Laser-nucleated acoustic cavitation: size matters

Bjoern Gerold^{1,2}, Joyce Joy¹, Oleg Prus², Javier Grinfeld², Alexander Volovick²,
Yaov Medan², Andreas Melzer¹, Sandy Cochran¹, Paul Prentice^{1*}

¹Institute for Medical Science and Technology,
University of Dundee, Dundee, DD2 1FD, UK

²InSightec Ltd, 5 Nahum Heth Street, Tirat
Carmel, 30120, Haifa, Israel

*corresponding author: p.prentice@dundee.ac.uk

ABSTRACT

We report on the development of an instrument for hybrid sono-optic cavitation studies. A focused ultrasound transducer is housed in a custom-built chamber, which permits optical access to the focal volume, without perturbing the propagating acoustic field. This configuration allows pulsed-laser irradiation of the liquid at the focus, and simultaneous high speed observation of cavitation activity in this region. In this paper we provide a brief description of the apparatus and present preliminary data on distinct cavitation regimes we have observed; specifically, laser-induced cavitation in an established field, and a new phenomenon that we refer to as *laser-nucleated acoustic cavitation*. The former involves a laser-pulse of energy above the threshold value for optical breakdown for the medium, in a pre-established ultrasound field. Here, a cavity rapidly expands to a maximum diameter of a few 100 microns, from the plasma generated on absorption of the optical energy, and collapses to form debris that is subsequently driven by the ultrasound radiation. By contrast, laser-nucleated acoustic cavitation is initiated by a pulse of energy below the ambient breakdown threshold, in a pre-established field. For this regime, either form of radiation does not result in cavitation activity without the other. In combination, the role of the laser-pulse is to initiate activity which is dominated by the ultrasound exposure from the outset. Crucially, the spatial and temporal precision afforded to the occurrence of cavitation by laser-nucleation, allows us to consolidate our assertion of acoustic cavitation. With observations at unprecedented resolutions, we compare the size of constituent cavities *within a single acoustical cycle* to theoretical predictions, based on the frequency of the ultrasound driving the activity. We also present preliminary results on the effects of ultrasound intensity on cloud formation and evolution. It is expected that such observations will contribute to a greater understanding of cavitation in focused ultrasound, including for potential future therapeutic applications.

NOMENCLATURE

f_c	transducer centre frequency
FOV	Field of View
FUS	Focused Ultrasound Surgery
HIFU	High Intensity Focused Ultrasound
LIC	Laser-Induced Cavitation
LNAC	Laser-Nucleated Acoustic Cavitation
Mfps	Megaframes per second (10^6 fps)
MHz	Megahertz (10^6 Hz)
mJ	millijoule
PNP	Peak Negative Pressure (amplitude)
R_f	Resonant bubble radius (to frequency, f)
R_{max}	Maximum bubble radius
R_{min}	Minimum (recorded) bubble radius
UCA	Ultrasound contrast agent (shelled microbubble suspensions)
US	Ultrasound

1. INTRODUCTION

1.1 Acoustic cavitation

Acoustic cavitation refers specifically to the formation and subsequent activity of bubbles, or cavities in the pressure fluctuations of an acoustic field, to distinguish from its mechanical or hydro-dynamical counterparts. The phenomenon is a common occurrence in the application of HIFU fields to the ablation of diseased tissue, known as FUS. In this emerging technique, ultrasound is focused transcutaneously to the site of pathology, thus alleviating the need for conventional surgical intervention, and reducing the associated risk of infection and patient recovery times. In current clinical procedure, the heating

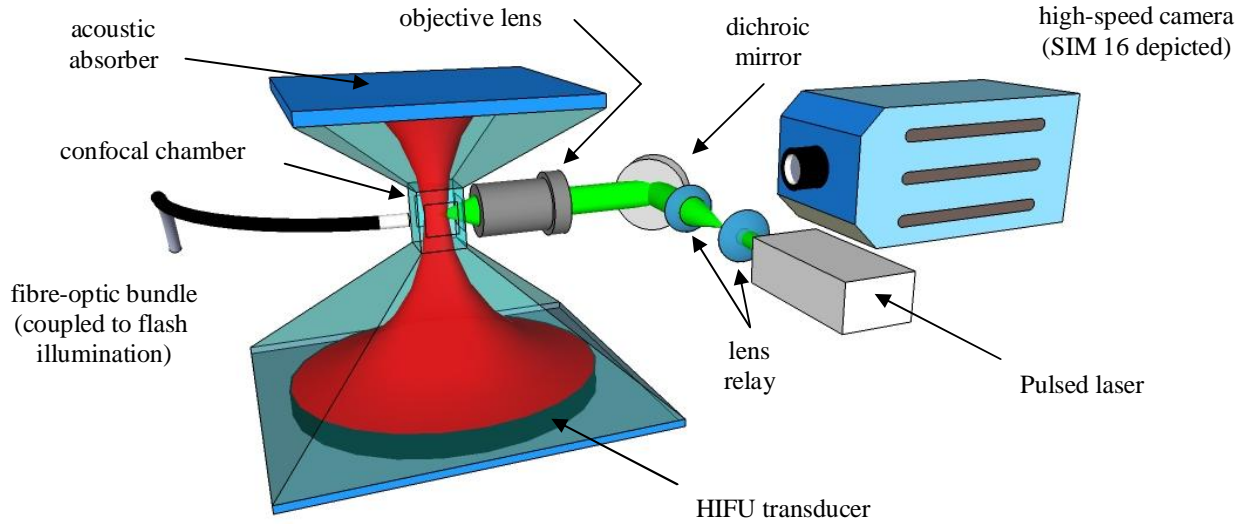


Figure 1. Schematic of experimental platform designed to combine laser and acoustic cavitation, with high speed observation capabilities. A focused-bowl transducer is housed within a custom-built sonoptic chamber, of dimensions dictated by the spatial distribution of the HIFU field generated, depicted red. The central confocal chamber contains the HIFU focal volume and incorporates optical windows for microscopic observation and pulsed-laser irradiation. High speed imaging may be performed with any camera of framing rate appropriate to the cavitation related activity being studied.

is achieved via viscous absorption of the mechanical energy [1], which is most intense at the focus, where the pressure amplitudes are the largest within the field. Heating also occurs in surrounding healthy tissue, such as in the near-field, but at levels that are not harmful, provided the exposure is not prolonged.

Acoustic cavitation occurs in FUS when the rarefactional tension imposed on the tissue during a negative pressure phase, is sufficient to form microscopic cavities, which fill with gas and vapor from the host medium. The occurrence of the phenomenon depends on a complex mix of the physical properties of the tissue, and the ultrasonic exposure parameters [1]. Continued HIFU excitation acts to further drive the bubble dynamics with a wide range of subsequent physical activity possible, including net growth through rectified diffusion, repulsion due to radiation forces, cloud formation via bubble-bubble interactions (fragmentation and coalescence), and free-radical production or sonochemistry (to mention but a few). It is generally recognized that cavitation in FUS has significant potential to mediate enhanced therapy, such as rapid tissue heating by trapping of the acoustic energy at the focus, or promoting drug delivery via tissue extravasation and microstreaming/pumping [2]. Translation of the phenomenon into medical practice is hampered, in part, by a fundamental lack of understanding of the rapid development of cavitation under HIFU exposure, and parallel development of acoustical detection techniques for monitoring and control purposes. Nonetheless, a growing body of literature demonstrates both

active and passive methods of acoustical cavitation detection, and correlation to cavitation related bio-effects in tissue [3], and tissue-mimicking materials [4]. The deficit in understanding cavitation evolution, particularly over the first few hundred acoustic cycles, stem from several inherent difficulties in studying the phenomenon *in-vitro*, including: (1) uncertainty in predicting the exact location within the field, and moment, of cavitation inception, (2) ultra-fast dynamics, driven at the MHz frequencies typical for FUS applications, and (3) cavities in MHz fields tend to be of the order of a few microns. This may be theoretically inferred with the simplified *Minnaert's equation* [5], for bubble radii, R_f resonant to a given ultrasound frequency, f_c , given by;

$$R_f \propto \frac{3}{f_c}$$

It may be appreciated that direct observational verification of bubble size is challenging for these reasons. Several studies have attempted to observe and characterize cloud evolution in HIFU fields with high speed cameras, for example [6]. The best high speed photography devices available are certainly capable of framing at the Nyquist sampling rate for MHz ultrasound, necessary to fully resolve dynamics. Microscopy objective lenses are also well capable of resolving objects on the micron scale. The researchers were, however, forced to image at spatial and temporal resolutions far below those necessary to make any meaningful observations of cavitation development. As such,

they were restricted to presenting images of established clouds on the millimeter scale, at 10 kHz sampling rates, with little impact on the understanding of the dynamical evolution.

Researchers have also resorted to less direct means for studying cavity sizes in acoustic fields. One such technique relies on sonoluminescence observations in pulsed ultrasound of varying inter-burst durations [7, 8], assuming quiescent bubbles dissolve over a period determined by the initial size. Brothie *et al* [8] developed the technique to report that resonant bubble radii in a 1056 kHz field increase with acoustic power, up to some threshold intensity, at which stage R_f stabilizes at $\sim 5 \mu\text{m}$.

Another approach, based on a similar principle, employed active ultrasonic scattering detection of bubbles, nucleated via HIFU induced destruction of ultrasound contrast agents, or UCAs [9]. The authors used acoustic scattering to measure resonant dissolution times for freed bubbles in a 1.1 MHz field - at pressure amplitudes similar to those of the present work - by comparing scattering patterns to models adjusted to account for the diffusivities of UCA core gases. Although they had to assume multiple size distributions to fit the data, features from the scattering amplitudes corresponded to R_f of 0.45, 1.2 and 1.56 μm .

1.2 Laser-induced cavitation

In contrast to its acoustic counterpart LIC is a very well characterized and understood phenomenon [10], with interest driven largely by ophthalmology applications. This owes to the reliability and reproducibility of employing laser-pulses to generate a cavity at a location, pre-defined by the focal point of a lens, used to concentrate the optical energy into the host medium. LIC studies have contributed greatly to the understanding of single cavity activity in particular, such as jet-formation in the presence of a boundary, and its dependence on the cavity-boundary distance [11]. Although the laser-medium interaction (and to an extent the resulting cavity, such as the degree of asymmetry that evolves) depends somewhat on parameters such as the pulse duration [12], it is well known that the process is plasma-mediated. Absorption of the optical energy at the focus causes localized weak breakdown to form a plasma, which rapidly expands to form a hot cavity of vapour and gas. The requirement for plasma formation imposes an energy threshold on the pulse, below which breakdown does not occur, and a cavity does not form. These factors also translate to a typical lower bound for the maximum diameter LIC bubbles can have, following the initial inflation stage of generally a few 100 microns, with millimeter sized bubbles being commonly investigated.

In this paper we describe a sonoptic chamber for hybrid laser-acoustic cavitation studies. LIC in an acoustic field has been reported before [13] where sonoluminescence from femtosecond laser-cavities in a 44.6 kHz stationary (standing) ultrasound field was studied as a function of seeding phase in an attempt to enhance collapse related phenomena (such as sono-chemical yield, perhaps). The investigators also used high speed photography to record increased and sustained expansion when the bubble was seeded such that maximum diameter coincided with a negative pressure phase. In this work, we use a

propagating HIFU field, and introduce cavitation activity by optically focusing a nanosecond laser-pulse into the US focal volume. We have found that reducing the pulse energy to below the breakdown threshold for the system, allows *cavitation nucleation*, without the characteristically large (relative to R_f determined by the field frequency) bubble formation associated with conventional LIC.

2. METHOD AND PROCEDURE

The hybrid laser-ultrasound experimental platform has been described in detail elsewhere [14], but a short overview is given here for completeness. Fig. 1 depicts the set-up schematically. The key feature is the sonoptic chamber that accommodates a HIFU field, the focal region of which can be irradiated with a laser-pulse and observed through a microscope objective lens. We employ a 3 nanosecond frequency-doubled neodymium-doped yttrium aluminium garnet (Nd:YAG) laser-pulse for cavitation induction and nucleation. The pulse is steered into the back aperture of a long working distance objective lens (Mitutoyo 50x 0.42 NA MPlan NIR ϕ -corrected), from a dichroic mirror reflective to the laser wavelength, 532 nm. The sonoptic chamber is custom-built to fit the HIFU field of a 1.47 MHz focused-bowl transducer, such that the field propagates unhindered by reflection or scattering of other than from cavitation intentionally introduced to the focal region.

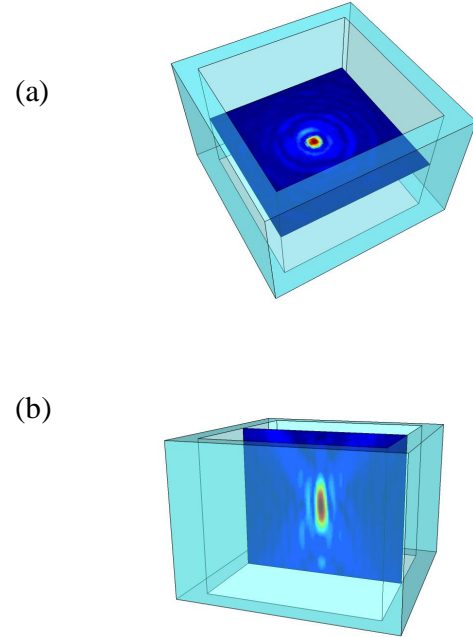


Figure 2. To scale representation of the (a) transverse, and (b) axial focus of the HIFU field, within the confocal region of the sonoptic chamber, which has dimensions: $20 \times 20 \times 14 \text{ mm}^3$. Higher peak pressures are indicated red, with ambient atmospheric pressure represented as deeper blue.

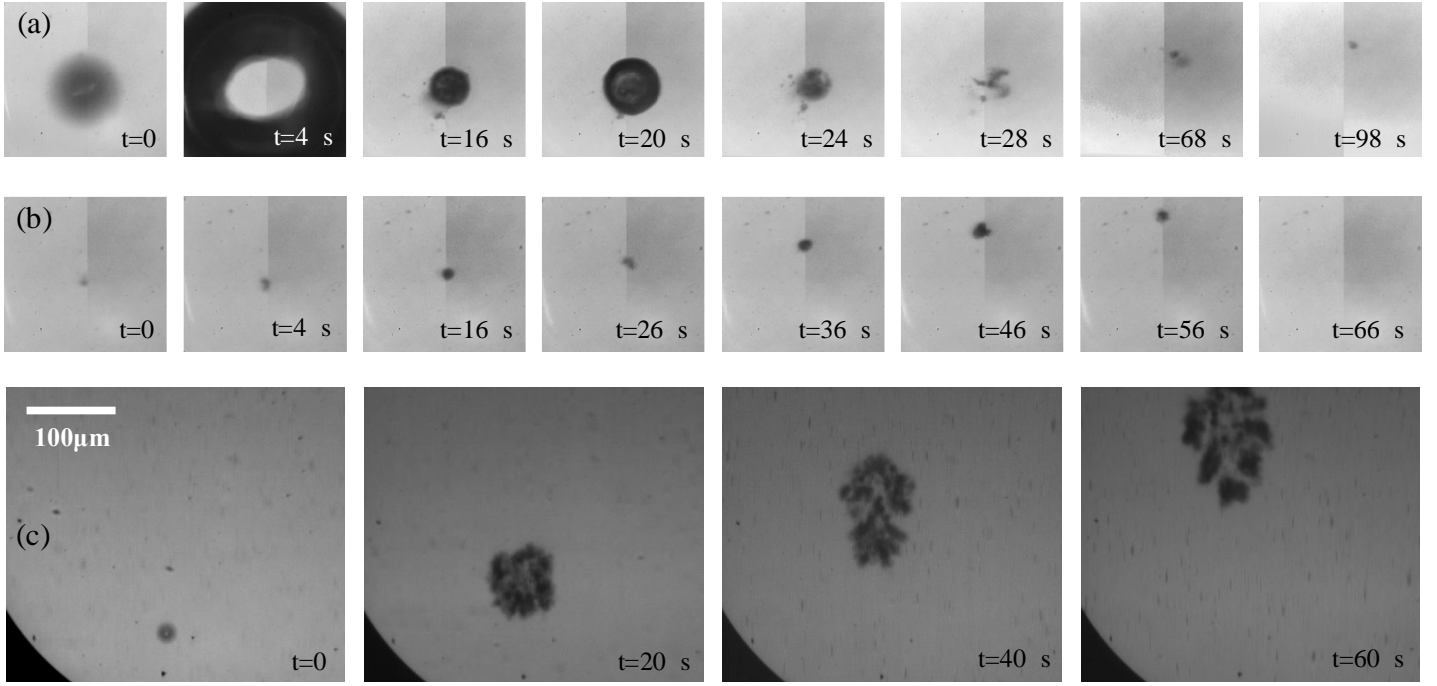


Figure 3. High-speed observations of hybrid laser-acoustic cavitation, extracted from sequences recorded at 0.5 Mfps. (a) A laser-pulse of energy *above the optical breakdown threshold*, is incident to the focal region of a relatively low intensity, pre-established HIFU field. (b) A laser-pulse of energy *below the breakdown threshold*, is incident to the same point, in an equivalent HIFU field to (a). (c) A laser-pulse of the same energy as (b) *below the breakdown threshold* is incident to the focal region of a significantly higher intensity HIFU field. Sequences (a) and (b) were captured through the 50x microscope objective lens, (c) through the 5x in the orthogonal configuration; the images have been resized to share a common scale. Image acquisition times are indicated, bottom right, with $t = 0$ s at time of laser-pulse generation.

In this way unwanted interference effects are avoided, and the focused ultrasound may be expected to propagate as it would in an idealised FUS procedure. Fig. 2 depicts the simulated US focus within the confocal chamber, where cavitation is instigated. The transducer is driven by a sinusoid signal from a function generator (Tektronix, USA) passed through an rf power amplifier (Electronics and Innovation, USA) and impedance matching network.

Alignment of the ultrasonic and laser foci is critical to reproducibility, and is achieved through schlieren imaging to visualise the ultrasound focus, and translation of the chamber (and transducer) to coincide with the laser spot [14]. A clicking sound becomes audible when alignment is complete, at a rate matching the pulse repetition frequency of the laser, signifying strong activity related to pulse generation. Cavitation dynamics are recorded with a high speed camera, imaging through either the same objective lens that focuses the laser-pulse (as depicted in Fig. 1), or a second lens (Mitutoyo 5x 0.14 NA MPlan APO \hat{O} -corrected) positioned orthogonally to the laser axis if a larger field of view is required.

Two high speed cameras were used for the collection of the data presented below, the Shimadzu HPV-1 and Cordin 550-62. The former is capable of 100 frames at up to 1 Mfps, the latter is a rotating drum device, offering 62 frames at up to 4 Mfps. The sensitive optics of the cameras were protected from scattered laser radiation with a green optical filter.

Quoted laser-pulse energies were measured at the back aperture of the objective lens with a power meter (ThorLabs, UK), and HIFU Peak Negative Pressure (PNP) amplitudes with a fibre-optic hydrophone (Precision Acoustics, UK). Spatial scales for the high speed images presented were determined by imaging flow cytometry beads, of diameters 10 and 50 microns, *in-situ*.

For an experiment, the laser is switched to single pulse mode and triggered from the high speed camera, with an appropriate delay for the Q-switch. The HIFU field is pre-established (turned on) 5-10 seconds before the laser-pulse is generated, and high speed photography initiated. All the results presented below used degassed tap water as the host medium.

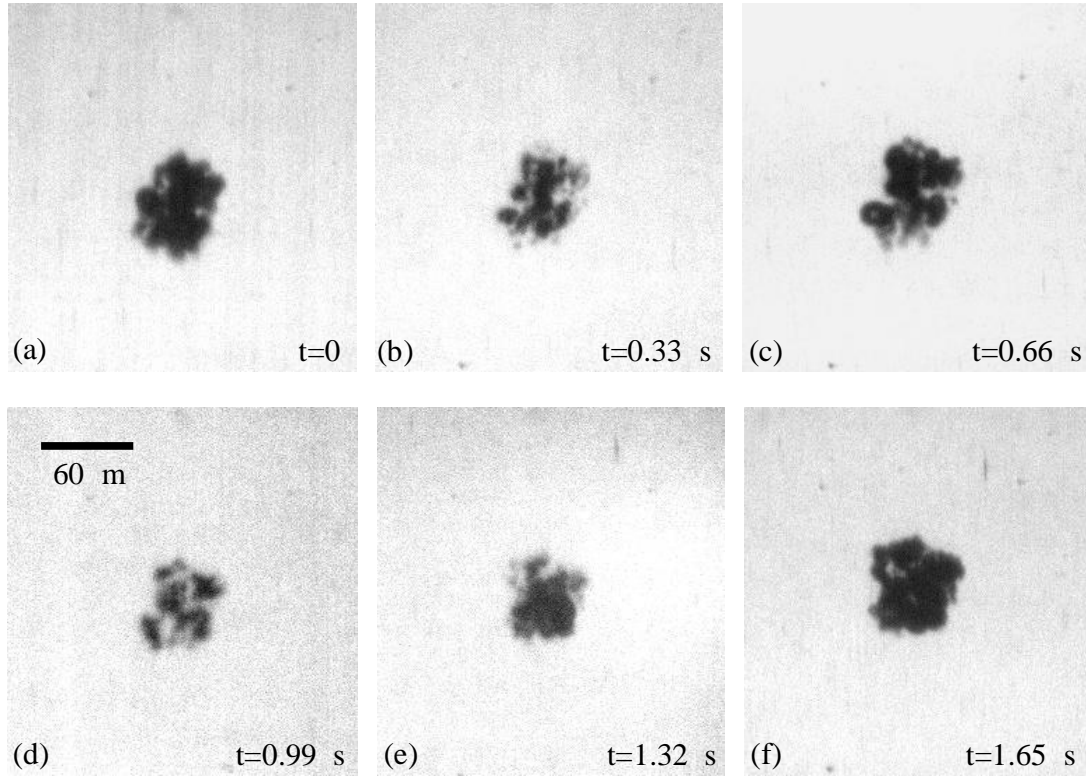


Figure 4. Consecutive frames extracted from a high-speed sequence of a developed LNAC cloud, in an intermediate intensity field, recorded at 3.05 Mfps. (a) A cloud of expanded cavities indicating a negative pressure amplitude phase for the incident ultrasound. (b) The cloud ~ 0.33 s later demonstrating cavity compression indicating a positive pressure phase. (c) ϕ (f) Continued cycling under the propagating HIFU pressure fluctuations. Image acquisition was through the 5x objective lens in the orthogonal configuration.

RESULTS AND DISCUSSION

Fig. 3 (a)-(c) represents the various forms of laser-acoustic cavitation that may be studied with the experimental architecture described. Sequence 3(a) is a recording of the cavitation activity that resulted from a 1.20 ± 0.02 mJ laser-pulse focused into the HIFU field with measured PNP = 1.3 ± 0.15 MPa (instrument error, according to manufacturer). The optical breakdown threshold for the system (without ultrasound radiation), defined as the pulse energy below which no LIC was observed, was determined to be 1.1 ± 0.4 mJ. The early stages of the dynamics are clearly dominated by LIC, with rapid bubble expansion to a diameter comparable to LIC without ultrasound radiation, $R_{\max} \leq 300$ μm . LIC collapse is accelerated by HIFU exposure, in comparison to LIC in the absence of ultrasound exposure. Moreover, the number of secondary rebounds and microbubble debris formation are also suppressed (data not shown, see reference [14]). Sequence 3(b) captures the cavitation activity resulting from a laser-pulse of 0.95 ± 0.02 mJ incident to the same location as in 3(a), and in an equivalent field.

Such a low energy laser-pulse *does not produce any cavitation activity, without the pre-established US field*. More than fifty tests were undertaken to confirm this. This sequence is representative of the minimal amount of cavitation activity we observed, which consists of a single small nucleus of $\ll 10$ μm , which proceeds to translate upwards, away from the HIFU transducer. As buoyancy is negligible over these timescales, we attribute this observation to the primary radiation force [5, 15]. We term this activity *laser-nucleated acoustic cavitation* (LNAC), to distinguish it from LIC in an established US field. Note that the translation speed is approximately constant throughout the sequence, and translation commences from the moment of nucleation. This is in contrast to the LIC in the pre-established field of 3(b), the centroid of which does not notably translate for the first ~ 30 μs .

Fig. 3(c) depicts LNAC with a pulse of 0.95 ± 0.02 mJ incident to the focal volume of the field with a PNP = 4.1 ± 0.5 MPa. As for sequence 3(b), absorption results in a small cavity nucleus that rapidly develops into a cloud of interacting cavities, which translate as a single entity away from the HIFU source.

Although the drag may be expected to be greater for this cloud than for the cavitation of 3(b), the translation speed is much higher due to the dependence of the radiation force on the square of the pressure amplitude [5,15]. To consolidate our assertion that fig. 3(c) is cavitation that is acoustic in nature, we now consider the size of the structural elements within the cloud. In fig 3(a-c) the imaging rate is less than the HIFU frequency, which is adequate to image cloud morphology evolution and translation, but insufficient to resolve component cavity dynamics. The relatively long exposure times used to capture these images result in objects becoming smeared over a region of pixels, as they oscillate under the influence of the incident US. As such, the best we can expect to infer is an upper bound on the maximum diameter during the oscillation. Moreover, this assumes no translation, coalescence, non-symmetrical dynamics etc, which is evidently not the case, and could lead to erroneous measurements.

Fig 4(a-f) are close-ups of six consecutive frames extracted from a sequence recorded at 3.05Mfps, at an advanced stage of LNAC cloud evolution, approximately 15.8 μ s following laser-pulse absorption and initial recorded cavitation activity. This sampling rate satisfies the Nyquist criterion for the 1.47 MHz HIFU frequency used, and as such allows quasi-resolved observation within a single acoustical cycle. Each frame represents an integration of the cavity dynamic over an exposure time significantly less than the inter-frame time of 0.33 μ s, compared to the duration of a negative or positive phase of the ultrasound, which at half the period is approximately 0.34 μ s. The HIFU driving this cavitation was of $P_{NP} = 2.20 \pm 0.26$ MPa. This mini-sequence records the cloud through just more than 2 cycles of US propagation. Intuitively, 4(a)-(c) was recorded during a negative-positive-negative cycle, with (d)-(f) capturing an expansion phase during a peak negative to peak positive transition. Fig. 4(d) in particular allows an upper limit to be put on the minimum radius, R_{min} , of some of the cavities within the cloud, of the order of a few microns. We estimate that equivalent features in the negative pressure phases of the incident US have R_{max} in the range of ~ 10 μ m. This would put many of the observable cavities at around the resonant size for the frequency used, in accordance with published literature. We also note that although the apparent translation under the action of the primary radiation force is much reduced from that observed in fig 3(c) - due to both reduced US intensity and increased frame rate for sequence acquisition - this might still result in a slight overestimate to the feature dimensions.

In conclusion, we have presented preliminary observations of a new technique that allows what appears to be predominantly acoustic cavitation to be nucleated, or seeded, by a nanosecond laser-pulse in a HIFU field. Crucially, the dominance of a large laser-induced bubble is avoided by reducing the pulse energy. The key advantage is the spatial and temporal precision the technique affords, which allows the incorporation of ultra-high speed micro-photography, at the resolutions required to observe cloud formation and evolution.

ACKNOWLEDGMENTS

The research leading to these results has received funding from the European Community's Seventh Framework Programme (FP7/2007-2013) under grant agreement n° 230674 (Nanoporation project). Bjeorn Gerold acknowledges support from a UK EPSRC Doctoral Training Award.

We are particularly grateful to Mr Adrian Walker and Mr Peter Collins of the EPSRC instrument loan pool, for continued access to various high-speed imaging devices. We acknowledge Dr Spiros Kotopoulos and Dr Michiel Postema for contributions to the development of the experimental platform and illuminating discussions. We also acknowledge Dr David M^cGloin and Dr Craig M^cDougal for provision of components and assistance with the laser set-up.

REFERENCES

- [1] ter Haar, G. Ultrasound focal beam surgery (1995) *Ultrasound Med. & Biol.* **21**(9) 1089-1100
- [2] Coussios, C. *et al* Role of acoustic cavitation in the delivery and monitoring of cancer treatment by high-intensity focused ultrasound (2007) *Int. J. Hyperthermia* **23**(2) 105-120
- [3] M^cGlaughlin, J. *et al* A study of bubble activity generated in ex-vivo tissue by high intensity focused ultrasound (2010) *Ultrasound Med. & Biol.* **36**(8) 1327-1344
- [4] Holt, R. & Roy, R. Measurements of bubble-enhanced heating from focused MHz-frequency ultrasound in a tissue-mimicking material (2001) *Ultrasound Med. & Biol.* **27**(10) 1399-1412
- [5] Leighton, T. *Acoustic Bubble* (1994) Academic Press, London
- [6] Chen, H. *et al* High-speed observation of cavitation bubble cloud structures in the focal region of a 1.2 MHz high-intensity focused ultrasound transducer (2006) *Ultrasonics* **14** 291-297
- [7] Lee, J. *et al* Determination of the size distribution of sonoluminescence bubbles in a pulsed acoustic field (2005) *J. Am. Chem. Soc.* **127** 16810-16811
- [8] Brothie, A. *et al* Effect of power and frequency on bubble-size distributions in acoustic cavitation (2009) *Phys. Rev. Lett.* **102** 084302
- [9] Chen, W. *et al* The disappearance of ultrasound contrast microbubbles: observation of bubble dissolution and cavitation nucleation (2002) *Ultrasound Med. & Biol.* **28** (6) 798-803
- [10] Fujimoto, J. *et al* Time-resolved studies of Nd:YAG laser-induced breakdown (1985) *Invest. Ophthalmol. Vis. Sci.* **26** 1771-1777
- [11] Brujan E. *et al* Dynamics of laser-induced cavitation bubbles near an elastic boundary (2001) *J. Fluid Mech.* **433** 251-281
- [12] Vogel, A. *et al* Shock wave emission and cavitation bubble formation by picoseconds and nanosecond optical breakdown in water (1996) *J. Acoust. Soc. Am.* **100** (1) 148-165
- [13] Kurz, T. *et al* Optic cavitation in an ultrasonic field (2006) *Phys. Rev. E* **74** 066307
- [14] Gerold, B. *et al* Laser-nucleated acoustic cavitation in focused ultrasound (2011) *Rev. Sci. Instr.* **82** (4) 044902
- [15] Palanchon, P. *et al* Optical observations of acoustical radiation force effects on individual air bubbles (2005) *IEEE UFFC* **52**(1) 104-110

Optical investigations of cavitating flow phenomena in micro channels using a nano second resolution

Uwe Iben^{*,a}, Alexander Morozov^{**,b}, Ernst Winklhofer^b, Romuald Skoda^a

^aRobert Bosch GmbH, Corporate Research and Advance Engineering - CR/ARH,
Postfach 106050, D-70049 Stuttgart, Germany

^bAVL List GmbH, Hans-List Platz 1, A-8020 Graz, Austria

* Uwe.Iben@de.Bosch.com

** alexander.morozov@avl.com

ABSTRACT

We have developed an optical measurement technique with a very high spatial and temporal resolution that allows the analysis as well as quantification of emitted shock waves and aggressive cavities that cause erosion.

By a pulsed transmitted light technique with an exposure time of 15 ns the collapse of either single bubbles or cavitation clouds can be detected and visualised. By laser pulsed interferometry based on an exposure time of 4 nano seconds the pressure values of the emitted shock waves are quantified. The results show a close interaction between the fluid properties, the bubble collapse events and the surrounding walls.

By our measurement technique, we can describe flow features of both, shear layer and acoustic cavitation. We describe the entire process between cavity generation, vapour bubble collapse, shock wave appearance and erosion location.

NOMENCLATURE

SYMBOLS

c	= Speed of sound	$[\text{m}\cdot\text{s}^{-1}]$
\dot{m}	= Mass flow rate	$[\text{kg}\cdot\text{s}^{-1}]$
p	= Pressure	$[\text{Pa}]$
r	= Distance	$[\text{m}]$
T	= Temperature	$[\text{K}], [^{\circ}\text{C}]$
u	= Velocity	$[\text{m}\cdot\text{s}^{-1}]$
ρ	= Density	$[\text{kg}\cdot\text{m}^{-3}]$

ABBREVIATIONS

BS	= Beam splitter
L	= Lens
M	= Mirror
$PREVERO$	= Experimental and CFD technology for preventive reduction of diesel engine emission caused by cavitation erosion
T	= Telescope
RMS	= Root mean square

SUBSCRIPTS

0	= Initial
in	= Inlet
out	= Outlet

1. INTRODUCTION AND MOTIVATION

Cavitation is the local evaporation of a fluid due to a pressure decrease below the vapour pressure¹. Furthermore, gas cavitation may occur due to the release of solved air if the pressure drops down below the saturation pressure. A two-phase mixture evolves which consists of liquid, vapour and dissolved gases. The cavities occur as small single bubbles or bubble clouds. The local properties of the mixture change dramatically with respect to the pure liquid, i.e. the density ratio between liquid and vapour can reach values between 10^3 and 10^4 . As a consequence, flow instabilities occur and the flow becomes highly transient. The time scales of evaporation as well as of condensation are in the nano second regime.

Cavitating flows occur in many hydraulic applications, e.g. in turbo and piston pumps, turbines and injection systems of combustion engines. The cavitation can usually not be avoided in most of the applications, but the geometrical properties of the application components can be optimized in a way that cavitation does not lead to erosion or that at least the system functionalities can be guaranteed. For the component design, the complete mechanism of cavitation and its interaction with the fluid flow has to be understood.

The collapse of single vapour bubbles or clouds can cause damages of walls. The collapse mechanism of single vapour bubbles is theoretically well-known, i.e. the collapse produces a shock wave with high amplitude, cf. [3]. The shock wave approaches the wall and causes a local deformation of it. It is also well-known that there are aggressive and non-aggressive cavities. The aggressiveness depends on the surrounding flow properties and the microscopic composition of the bubble clouds, cf. [2]. If the cavity enters a flow domain with high

¹ We assume that cavitation starts below the vapour pressure and the fluid does not contain tensile stress.

pressure, it collapses very quickly and emits strong shock waves which interact with the flow itself and with the walls. The interaction of the pressure forces and inertia forces of the fluid can produce very complex flow structures on different time scales.

The collapse of single cavities generated by laser light has been studied in several works, cf. [1, 5, 7]. In the majority of the cases, single latent bubbles and their collapse have been investigated by a Schlieren or photograph technique. Investigations of cavitation in micro geometries with high pressure differences have been started in the PREVERO project². The experimental PREVERO methods such as interferometry and transmitted light technique have been continuously developed and applied to the different technical applications in the past years.

The present paper presents a refined experimental study of properties of cavitating flows in a micro geometry with optical methods with very high spatial and temporal resolution. We present the application of an interferometry technique with a temporal resolution of a few nano seconds on a throttle flow with a downstream located test (or ‘target’) body. Using very short exposure times, the collapse of cavities and the shock wave emission can be observed. The fluid is the test oil V1404 whose properties such as density in dependence on pressure p and temperature T are well-known.

This paper is organized as follows: In Section 2 the experimental setup and the procedure are described. The results are discussed in Section 3. A summary and an outlook are given in Section 4.

2. EXPERIMENTAL SETUP AND PROCEDURE

2.1 Test facility

The experimental facility includes a pressure supply system, the high-pressure throttle, a back flow circuit as well as measurement sensors and devices, cf. [4]. The hydraulic system is designed to supply well-defined in- and outflow conditions to the high-pressure throttle. The system supports variable and precisely controlled macroscopic boundary flow conditions, i.e. the inlet pressure p_{in} , the inlet temperature T_{in} and the outlet pressure p_{out} . In addition to p_{in} , T_{in} and p_{out} the measurement of the outlet temperature T_{out} and the time-averaged mass flow rate \dot{m} is done. A variable inlet pressure with pressure fluctuations smaller than 1 bar is realised.

The channel geometry that is to be investigated has been cut in a plane steel plate with a thickness of 300 μm . It is sandwiched between two sapphire windows. One window includes the hydraulic inflow as well as the hydraulic outflow where the pressures and the temperatures are measured.

The high-pressure throttle with the flow path is illustrated in Fig. 1a together with a sketch of the studied hydraulic test geometry Fig. 1b. The test geometry contains an inflow channel which is 3 mm high, the throttle itself and a test body behind the throttle and is based on former investigations done in the

PREVERO project. In contrast to these former investigations, the optical methods and analyzing algorithms have been significantly improved. The former exposure time was limited to values not lower than 100 ns for the transmission light and 400 ns for the interferometry technique, and therefore shock waves could not be resolved. Meanwhile the measurement technique has been improved in a way that turbulent flow structures and single cavities can be observed.

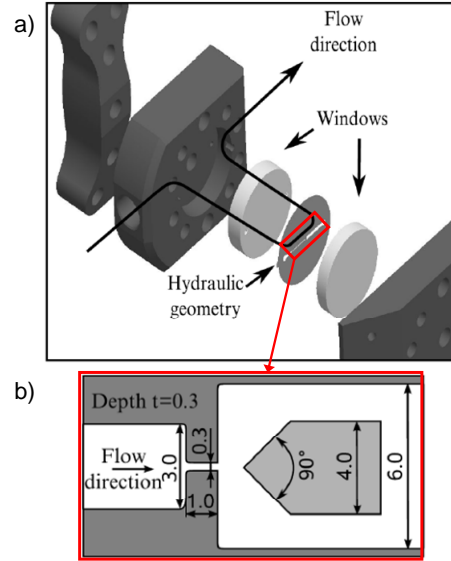


Fig. 1: Test geometry, cut out of a steel plate with an outer diameter of 60mm and a depth of 300 μm . The geometrical dimensions are specified in [mm]

2.2 Visualization with the transmitted light technique

The visualization is done with the transmitted light technique where a Nanolite light source with pulse duration of 15 ns is used. The light beam passes the optical windows, and the vapour and gas bubbles scatter the light in a way that they appear as dark regions on the image. On the other hand, the light passes the uniform one-phase liquid without any scatter so that no shading is visible on the image. The flow inhomogeneities due to density gradients and shock waves are visible as grey areas. This technique allows a qualitative analysis of fluid flows with cavities and density gradients, such as shock waves emitted by collapsing cavities [4]. The frame rate is limited by 5 Hz, so that only single flow events can be visualized. Due to the low frame rate these single flow events are statistically independent. For each operating condition a sequence of one hundred images has been recorded and the corresponding mean transmission and standard deviation (RMS) spatial distributions have been calculated. We call this mean transmission ‘cavitation probability’. Both, cavitation probability and RMS are determined for the entire flow field that is under investigation. We obtain a spatial resolution of 3 μm in the object plane. Assuming a sound speed of 1200 $\text{m}\cdot\text{s}^{-1}$, we receive a shock wave displacement during exposure time corresponding to a few camera pixels at the image plane.

Note that the transmitted-light technique yields a depth-average representation of the flow field.

² Project funded by the European Union 2003-2005

2.3 Laser-pulsed interferometry

In order to analyse the density and pressure field in a quantitative way, the laser-pulsed interferometry measurement technique has been developed by the authors, cf. [4]. Due to the very high spatial (3 μm) and temporal (5 ns) resolution this technique is applied to the diagnostics of shock waves in the liquid. The experimental setup is shown in Fig. 2. We use the following linear approximation of the thermodynamic equation of state for the liquid, i.e.

$$\rho(p, T) \approx \rho(p_0, T_0) + \left. \frac{\partial \rho}{\partial p} \right|_{(p_0, T_0)} \cdot (p - p_0) + \left. \frac{\partial \rho}{\partial T} \right|_{(p_0, T_0)} \cdot (T - T_0) \quad (1)$$

Eq. (1) allows the determination of the pressure distribution from the measured density distribution with the assumption of a locally constant temperature. The coefficients in eq. 1 have been determined for the test fluid in former studies [4]. The index 0 defines the reference point where the density (pressure, temperature) values are known by means of another independent measurement technique.

As for the transmission light technique, the frame rate equals 5 Hz. The interferometric images together with image evaluation techniques provide the ensemble of single-shot pressure fields, mean pressure field data, local pressure fluctuation and differential pressure data. This yields information about local flow features such as flow vortex generation frequency, spatial size and shape of vortices and local pressure distribution inside of vortex structures. Features of bubble collapse process and corresponding pressure shock waves in the liquid have been observed and analyzed.

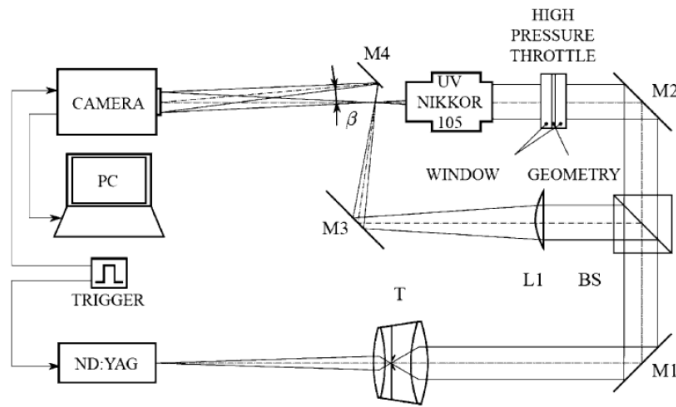


Fig. 2: Experimental setup with optical components and data acquisition tools; T: telescope, M1,...,M4: mirrors, L1: lens, BS: beam splitter

2.4 Experimental procedure

The time-integrated mass flow curve dependence on the pressure difference $\Delta p = p_{\text{in}} - p_{\text{out}}$ is determined by a Coriolis mass flow meter. The inlet pressure is fixed at $p_{\text{in}} = 300$ bar and the inlet temperature at $T_{\text{in}} = 306$ K. The high pressure part is

designed in a way that the pressure oscillations at the inlet are smaller than 1% which corresponds to the measurement accuracy of the pressure sensors. The outlet pressure is varied in the range $p_{\text{out}} = 200$ bar to 20 bar. The outlet part contains a chamber in order to damp the pressure waves. Fig. 3 depicts the mass-flow curve via pressure difference Δp for an inlet temperature $T_{\text{in}} = 306$ K consisting of the Bernoulli-part (linear part with positive slope) and the choked flow (constant mass flow). The point of intersection of both curve parts is dependent on the inlet shape of the throttle.

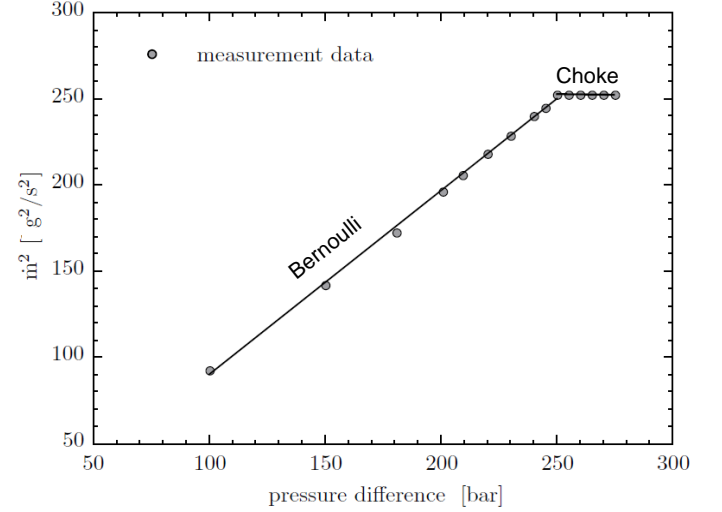


Fig. 3: Mass flow curve: inlet pressure $p_{\text{in}} = 300$ bar, inlet temperature $T_{\text{in}} = 306$ K and variable outlet pressure

3. RESULTS AND DISCUSSION

In this section we show that cavitation causes a very strong interaction between acoustic phenomena such as pressure and shock waves and flow phenomena such as turbulence.

3.1 Former results

Fig. 4 shows the erosion findings after 120 min, 140 min and 150 min of operation time for an outlet pressure of $p_{\text{out}} = 20$ bar. The unbalance of the erosion location is due to a weak unbalance of the target position with respect to the throttle. According to these results of the PREVERO project, aggressive cavities in front of the target produce the depicted material erosion. For these measurement series, shock waves due to the collapse of cavities could not be observed due to the long exposure time of 100 ns and the erosion mechanism could not be analyzed by the available optical methods at this time due to the same reason.

Nevertheless, in addition to the erosion findings, the mean values of cavitation probability and the corresponding RMS have been computed by analyzing statistically independent images. As an example, recent results at the same conditions for the cavitation probability and the RMS are presented in Fig. 5. The empirical rule has been derived that the erosion start location coincides with the location of the maximal RMS value near the eroded surface. The target material (aluminium) erosion

was measured at relatively low $p_{\text{out}} = 20$ bar, which corresponds to shear layer cavitation and choked flow within the throttle.

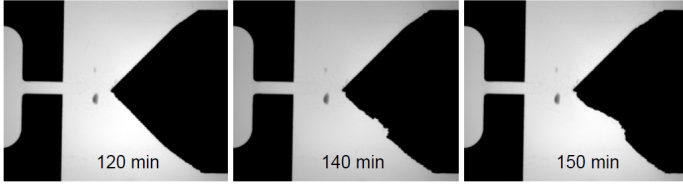


Fig. 4: Erosion on the target after 120 min, 140 min and 150 min:
 $p_{\text{in}} = 300$ bar, $p_{\text{out}} = 20$ bar, $T_{\text{in}} = 338$ K

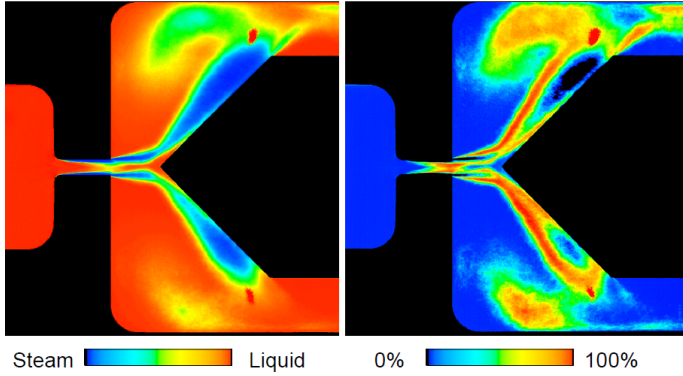


Fig. 5: Cavitation probability (left) and RMS (right) for $p_{\text{in}} = 300$ bar, $p_{\text{out}} = 25$ bar, $T_{\text{in}} = 306$ K

3.2 Results based on transmitted light technique

With the enhancement of the measurement technique, i.e. a shorter exposure time and a higher optical resolution, shock waves can now be resolved and observed. We did flow visualisation measurements for a broad range of $p_{\text{out}} = 20 \dots 200$ bar. Some selected results of the calculated RMS distribution are presented in Fig. 8. The analysis shows that at low p_{out} shear layer cavitation occurs within the throttle, in the free jet behind the throttle as well as near the lower and upper front surfaces of the target. Growing p_{out} from 20 bar to 50 bar causes the decrease of the cavitation probability together with the corresponding RMS (choked flow part of hydraulic curve, Fig. 3). For a further growth of p_{out} from 50 bar to 120 bar (which is already in the Bernoulli part of the mass flow curve) the cavitation probability diminishes permanently, but the RMS values remain relatively large with some changes of location. Further increase of $p_{\text{out}} > 120$ bar corresponds to a monotone decrease of both, cavitation probability and RMS in the entire flow field.

We identify the particular kind of cavitation phenomena that we have observed between 50 bar and 160 bar as acoustic cavitation which is quite different from shear layer cavitation.

In order to study the acoustic cavitation in more detail, we consider cases with two distinct outlet pressures $p_{\text{out}} = 90$ bar and $p_{\text{out}} = 121$ bar (Fig. 6 and 7). We observe flow instabilities indicated by orderless patterns inside the free jet between the throttle exit and the target front. Furthermore, shock waves can

be discerned and are more frequent for $p_{\text{out}} = 90$ bar than for $p_{\text{out}} = 121$ bar.

We have found out that the most aggressive operation point with respect to cavitation erosion corresponds to an outlet pressure of $p_{\text{out}} = 121$ bar. In fact, during the recent experimental procedure, the sapphire windows were eroded for $p_{\text{out}} = 121$ bar within several minutes (see Fig. 7 and 8).

At $p_{\text{out}} \leq 110$ bar we observe shock waves that are not as strong as at $p_{\text{out}} = 120$ bar and at $p_{\text{out}} \geq 130$ bar shock waves occur less frequently.

A thorough observation of the results for the operation point $p_{\text{in}} = 300$ bar and $p_{\text{out}} = 90$ bar and 121 bar allows the following summary (Fig. 6 and 7):

- A laminar inflow to the throttle - no flow structures (density gradients) are visible. The Reynolds number is ≈ 700 in this domain.
- Shear layers and small turbulent structures at the lower and upper side of the throttle. A laminar flow is inside the throttle.
- An instable free turbulent jet downstream of the throttle. The stagnation point at the target turns up and down.
- If the free jet turns up, the pressure decreases in the lower fluid domain (this fact is illustrated in Fig. 9 for a different outlet pressure $p_{\text{out}} = 157$ bar) so that cavities occur. These cavities show up as single bubbles or clouds of different sizes. Cavities at the positions marked with crosses in Fig. 6 occur frequently and are associated with the erosion damage due to acoustic cavitation. These cavities are located in a fluid domain with low flow velocities and are provoked by rarefaction waves. At the same time the pressure has increased in the upper half of the domain, and the cavities in this upper domain part collapse. For $p_{\text{out}} = 121$ bar (Fig. 7), the shock waves are so strong that they cause erosion on the sapphire windows within a very short time period of two minutes at the positions marked with crosses in Fig. 6.
- If the free jet turns down, the reverse procedure takes place. The flow is transitional due to the alternating interaction with the laminar flow field and the turbulent jet wake.
- Downstream, the flow is laminar again.

These periodical events of formation and collapse of cavities are illustrated in Fig. 6 and Fig. 7 as a sequence of four images. The two dark regions marked with the cross show the locations of periodically occurring and vanishing vapour clouds as well as the positions of erosion on the sapphire plates. As soon as the hydraulic operation point has been set-up the sapphire windows are damaged within two minutes.

The spatial RMS distributions for four outlet pressures are shown in Fig. 8. Positions where we have found erosion – on the target for $p_{\text{out}} = 25$ bar and on the sapphire windows for $p_{\text{out}} = 121$ bar – are regions with high RMS values that correlate well with the erosion locations. The red arrow marks the erosion on the sapphire windows (Note that the sapphire window damages stem from the operation point with $p_{\text{out}} = 121$ bar.). An analysis

of the RMS value at the exact damage positions of the sapphire windows is not possible. Nevertheless, the typical tendency is visible.

We observe high RMS values also for $p_{\text{out}} = 90$ bar. However, for this operation point no damage occurs. We assume the absence of the damage due to the lower pressure level and conclude that both, a sufficiently high RMS and pressure level are necessary to cause an erosion damage.

The transmitted light images show in an impressive way the flow structures with its cavities and shock waves. However, a statement on the density or pressure values inside the fluid domain is only possible with interferometry measurements.

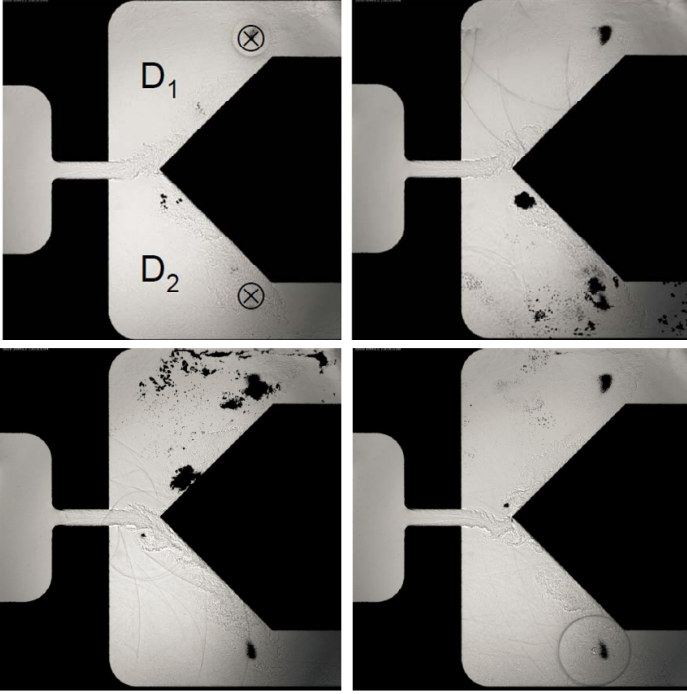


Fig. 6: Transmitted light images for different time instances for $p_{\text{in}} = 300$ bar, $p_{\text{out}} = 90$ bar and $T_{\text{in}} = 342$ K

3.3 Results based on laser-pulsed interferometry

For a quantitative flow field description, we apply our high-resolving interferometry measurement technique and analyze single shot pressure distributions. The exposure time is fixed at 5 ns and the spatial resolution is 3 μm . Details of the measurement technique are described in [4].

We observe strong pressure variations (± 150 bar) at the upper and lower regions of the target flow which in particular can cause very low local pressure levels in the region below and above the target tip, e.g. the pressure can fall below the vapour pressure and therefore cavitation can occur.

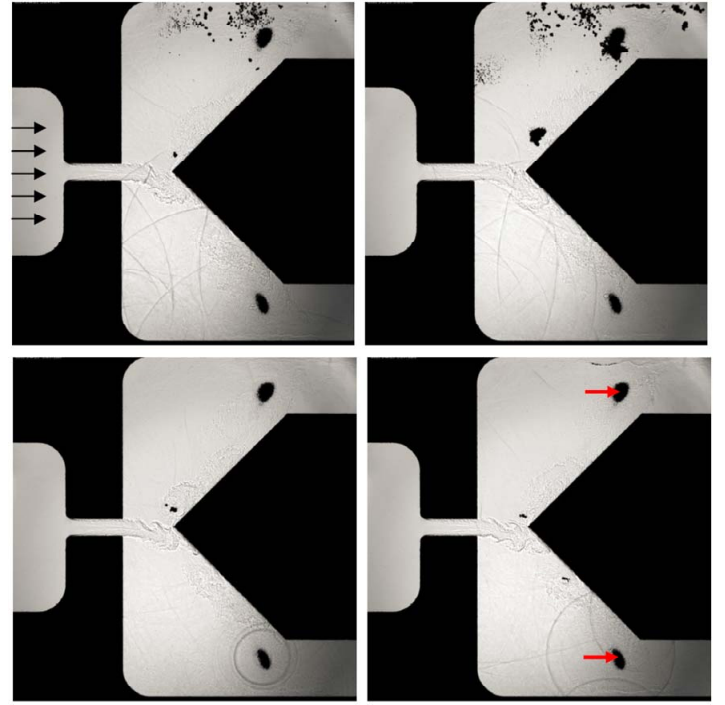


Fig. 7: Transmitted light images for different time instances for $p_{\text{in}} = 300$ bar, $p_{\text{out}} = 121$ bar and $T_{\text{in}} = 342$ K.

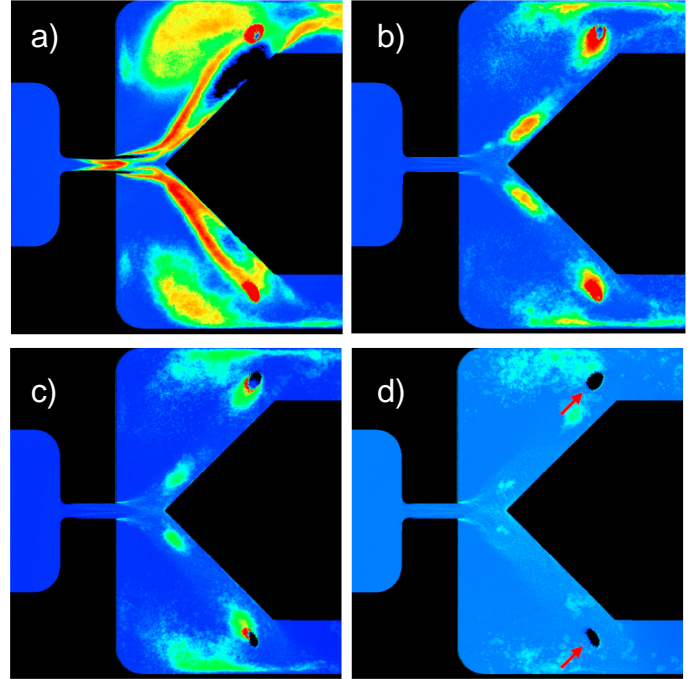


Fig. 8: RMS distribution for four different time instances for, a) $p_{\text{out}} = 25$, b) $p_{\text{out}} = 90$, c) $p_{\text{out}} = 121$ and d) $p_{\text{out}} = 151$ bar; $p_{\text{in}} = 300$ bar and $T_{\text{in}} = 342$ K. Note that the damages on the sapphire windows marked in Fig. 8 d) stem from the operation point $p_{\text{out}} = 121$ bar, corresponding to the flow field illustrated in Fig. 8 c.

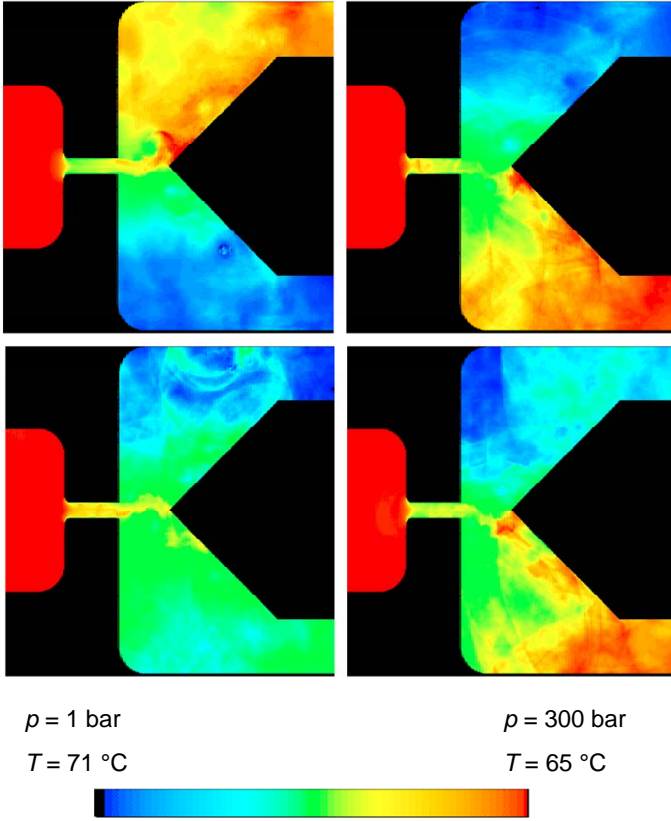


Fig. 9: Pressure distribution at different instances for $p_{\text{in}} = 301 \text{ bar}$, $p_{\text{out}} = 157 \text{ bar}$ and $T_{\text{in}} = 338 \text{ K}$

We have seen that with the fluctuation of the free jet and the motion of the stagnation point, the pressure changes significantly in the points that are marked “D1” and “D2” in Fig. 6. Even if we consider a rather high outlet pressure $p_{\text{out}} = 157 \text{ bar}$ (Fig. 9), the pressure reaches values greater 300 bar alternatively in the points D1 and D2. Consequently, strong alternating forces affect the target.

Fig. 10 contains the pressure distribution of the complete flow field (above) and a detailed representation of the pressure field inside the throttle (below). A shock wave induced by a collapsing cavity travels through the throttle against the flow direction. The amplitude of the shock wave is in the range of the inlet pressure.

The interferometry measurement technique also allows the measurement of the emitted pressure waves provoked by collapsing cavities. Fig. 11 shows the interferogram and the pressure distribution around a pressure wave. The amplitude of the pressure wave diminishes with $1/r$, where r is the distance of the wave from the centre of the collapsed cavity and equals in the depicted example $r \approx 150 \text{ }\mu\text{m}$. The size of the cavity itself equals about $10 \text{ }\mu\text{m}$. Thus, the amplitude of the impact pressure instantaneously after the collapse can be estimated as to be about 900 bar.

4. SUMMARY AND OUTLOOK

Transmitted light technique and laser-pulsed interferometry using a resolution in the nano second regime have been applied to analyze the cavitating flow field within a simple planar micro geometry. The experiments have shown:

- Shock waves induced by collapsing cavities can be observed and analyzed by the optical measurement technique presented here.
- Different hydraulic operation points produce different erosion locations in the test geometry.
- Shock waves induced by collapsing cavities can travel against the flow direction to the inlet and the outlet of the geometry. Therefore, all components of the hydraulic system communicate by pressure waves.
- The position of erosion depends on the pressure difference. We find erosion on the target for an outlet pressure $p_{\text{out}} = 20 \text{ bar}$. Isolated and periodically occurring cavities produce erosion on the sapphire windows for an outlet pressure $p_{\text{out}} = 121 \text{ bar}$.

These observations are compliant to theoretical investigations done by [2] and [6]. Furthermore, the experimental results can be utilised to validate simulation methods. A further improvement of the optical path will follow in a next step. It will allow the analysis of the amplitude of the shock wave in detail, i.e. the determination of the pressure amplitude a few nano seconds after the collapse of the cavities. A further installation of a double-pulse laser interferometry will allow the analysis of the temporal evolution of shock waves.

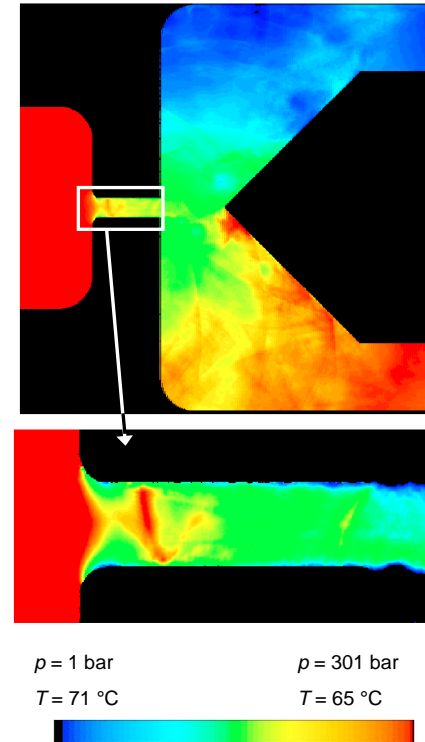


Fig. 10: Shock wave travel against the flow direction within the throttle: $p_{\text{in}} = 301 \text{ bar}$, $p_{\text{out}} = 157 \text{ bar}$ and $T_{\text{in}} = 338 \text{ K}$

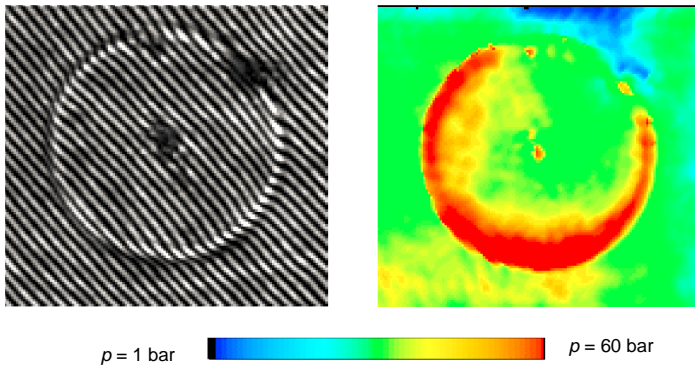


Fig. 11: Interferogram (left) and pressure distribution (right) of a single cavity: $p_{\text{in}} = 301$ bar, $p_{\text{out}} = 157$ bar and $T_{\text{in}} = 338$ K. On the right hand side, pressure values relative to the time-averaged image are shown.

REFERENCES

- [1] N. Bidin. Shock wave emission during cavitation bubble collapse in free liquid. *Pertanika J. Sci & Technol.*, 3(1):51–55, 1995.
- [2] C. Brennen, G. Reisman, and Y.-C. Wang. Shock waves in cloud cavitation. In *Twentyfirst symposium on Naval Hydrodynamics*, pages 756–771, 1997.
- [3] J.-P. Franc and J.-M. Michel. *Fundamentals of cavitation*. Kluwer Academic publisher, 2005.
- [4] U. Iben, A. Morozov, E. Winklhofer, and F. Wolf. Laser-pulsed interferometry applied to high-pressure fluid flow in micro channels. *Exp. Fluids*, 50:597–611, 2011.
- [5] W. Lauterborn, T. Kurz, C. Schenke, C.-D. Ohl, R. Geisler, and O. Lindau. Shock waves from cavitation bubbles. *J. Acoust. Soc. Am.*, 105, 1999.
- [6] A. Philipp and W. Lauterborn. Cavitation erosion by single laser-produced bubbles. *J. Fluid Mech.*, pages 75–116, 1998.
- [7] A. Vogel, S. Busch, and U. Parlitz. Shock wave emission and cavitation bubble generation by picosecond and nanosecond optical breakdown in water. *J. Acoust. Soc. Am.*, 100:148–165, 1996.